

Fault Friction Derived from Fault Bend Influence on Coseismic Slip During the 2019 Ridgecrest M_w 7.1 Mainshock

Authors: Milliner, C.W.D^{1*}, Aati, S.¹, Avouac, J.P.¹

¹ *California Institute of Technology, Pasadena, CA*

**corresponding author: milliner@caltech.edu, @Geo_GIF*

This manuscript has been accepted for publication in Journal of Geophysical Research: Solid Earth. When available, the final version of this manuscript will be found via the 'Peer-reviewed publication DOI' link on the EarthArxiv web page.

1 **Title:** Fault Friction Derived from Fault Bend Influence on Coseismic Slip During
2 the 2019 Ridgecrest M_w 7.1 Mainshock

3
4 **Authors:** Milliner, C.W.D¹, Aati, S.¹, Avouac, J.P.¹

5
6 ¹ California Institute of Technology, Pasadena, CA

7
8 **Abstract**

9
10 The variation of stress on faults is important for our understanding of fault friction and the
11 dynamics of earthquake ruptures. However, we still have little observational constraints on their
12 absolute magnitude, or their variations in space and in time over the seismic cycle. Here we use a
13 new geodetic imaging technique to measure the 3D coseismic slip vectors along the 2019
14 Ridgecrest surface ruptures and invert them for the coseismic stress state. We find that the
15 coseismic stresses show an eastward rotation that becomes increasingly transtensional from south-
16 to-north along the rupture, that matches the known background stress state. We find that the main
17 fault near the M_w 7.1 mainshock hypocenter was critically stressed. Coseismic slip was maximum
18 there and decreased gradually along strike as the fault became less optimally oriented due its
19 curved geometry. The variations of slip and stress along the curved faults are used to infer the
20 static and dynamic fault friction assuming Mohr-Coulomb failure. We find shear stresses of 4-9
21 MPa in the shallow crust (~ 1.3 km depth) and that fault friction drops from a static, Byerlee-type,
22 value of 0.61 ± 0.14 to a dynamic value of 0.29 ± 0.04 during seismic slip. These values explain
23 quantitatively the slip variations along a transpressional fault bend.

24
25 **Keywords:** Stress, friction, Ridgecrest, geodesy

26
27 **Plain Language Summary:**

28 Understanding the orientation and magnitude of stresses within the crust are important because
29 they can affect the location, size and spatial extent of earthquake rupture. However, measuring the
30 absolute magnitude and orientation of stresses as well as the frictional properties of the fault
31 surface (i.e., how strongly the fault resists the applied driving forces) is very difficult. Here we use

32 optical images acquired by satellites to measure how the surface deformed in 3D during the 2019
33 Ridgecrest event. These 3D measurements allow us to extract the direction of fault slip movement
34 along the entire rupture length which we use to estimate the direction of stresses by assuming the
35 shear stress is parallel to the direction of the observed fault slip motion. We find that the main fault
36 near the mainshock epicenter was the most optimally aligned for failure, which could be one
37 contributing reason for the location of rupture initiation. By deriving a relation between how much
38 a fault slips with how well aligned it is to the stress field we can estimate the absolute magnitude
39 of stresses, the frictional resistance at initial fault sliding (finding a static friction = 0.61) and
40 during sliding (a dynamic friction = 0.29).

41

42

43 **Keypoints:**

- 44 1. Inverting surface coseismic slip vectors show a variable stress state that matches the
45 background stresses constrained by seismicity
- 46 2. Faults at the mainshock epicenter were the most critically stressed; we find slip increases
47 linearly as faults become more optimally aligned
- 48 3. We find absolute stress magnitudes of 8-26 MPa in the upper crust, a static frictional
49 coefficient of 0.61 and a dynamic value of 0.29

50

51 **1.0 Introduction**

52

53 Earthquakes are frictional slip instabilities which initiate when the applied shear stress exceeds the
54 yield strength of the fault. During sliding the friction can increase (dynamic strengthening) or
55 decrease (dynamic weakening), where the former inhibits rupture, and the latter can sustain a
56 runaway failure which relieves a fraction of the accumulated stress along the fault surface. During
57 the interseismic period the elastic stresses re-accumulate along the locked fault surface until the
58 fault strength is reached again and another earthquake occurs. This basic description of the seismic
59 cycle underlines the importance of fault strength in our understanding of when and how
60 earthquakes occur. However, outstanding questions remain regarding the strength of faults
61 including, is the frictional strength substantially lower during rupture than the static strength
62 expected for a standard value of the static coefficient of friction (the ratio of the shear to normal

63 stress) which is generally around 0.6 for most rocks) (Byerlee, 1978)? If so, what is the extent of
64 dynamic weakening? Are faults inherently weak or are intracrustal faults stronger than their more
65 mature plate boundary counterparts? In this study we attempt to place empirical constraints on
66 these important fault mechanical properties using observations of a surface rupturing event
67 provided by satellite imaging data.

68 The 2019 Ridgecrest earthquake sequence initiated on July 4th by a series of foreshocks
69 which later ruptured a series of orthogonal faults near the city of Ridgecrest located north of the
70 Mojave Desert (Ross et al., 2019). First, a M_w 6.4 event ruptured a dextral NW-trending fault at
71 depth and a sinistral NE-trending fault at the surface. This was then followed ~34 hours later by
72 the M_w 7.1 mainshock that initiated ~15 km to the north. During the mainshock event, kinematic
73 source models show a transition from an initially crack-like to pulse-like bi-lateral rupture (Fig.
74 1). The rupture then evolved to an unilateral slip pulse which propagated southeastwards at a
75 relatively slow velocity of ~2 km/s along a curved 19° compressional fault bend (Fig. 1c) (Ross *et*
76 *al.*, 2019; Chen *et al.*, 2020; Goldberg *et al.*, 2020). Measurements made in the field or from
77 satellite image correlation (Barnhart, Hayes and Gold, 2019; Ponti *et al.*, 2019; DuRoss *et al.*,
78 2020; Milliner and Donnellan, 2020; Antoine *et al.*, 2021; Gold, DuRoss and Barnhart, 2021) show
79 a gradual decrease of coseismic slip (~2.5 m over a ~5 km distance) southwards and away from
80 the mainshock epicenter along the curved fault geometry (see fault bend location in Fig.1). In this
81 study we analyze how this feature relates to fault stress and show that some information on fault
82 friction can be derived.

83 Previous studies using focal mechanisms from background seismicity and
84 aftershocks have provided estimates of the state of stress in the crust around the Ridgecrest region,
85 including its spatial variation along the foreshock and mainshock ruptures and its change with
86 time. Inversion of focal mechanisms from background seismicity prior to the 2019 earthquake
87 sequence shows a strike-slip stress regime along the faults involved in the mainshock rupture
88 (where the intermediate compressive principal stress [σ_2] is approximately vertical) with some
89 spatial variations along-strike (Hardebeck, 2020; Hauksson *et al.*, 2020; Sheng and Meng, 2020;
90 Wang and Zhan, 2020). The maximum principal stress, σ_1 , is near-horizontal and rotates from due
91 North at the southern end of the mainshock rupture to ~N12°E in the north. The stress shape ratio
92 (R), which characterizes the relative magnitudes of the principal stresses and is defined as $R =$
93 $[\sigma_1 - \sigma_2]/[\sigma_1 - \sigma_3]$, also spatially varies and indicates an increasingly transtensional stress

94 regime to the north. Here we attempt to assess how spatially variable the stresses are that are
95 released along a rupture and whether this supports the notion of heterogeneity of the stress
96 orientation at the ten's of kilometers scale in the surrounding crust that is typically inferred from
97 background seismicity.

98 Hereafter we introduce the tectonic setting of the Ridgecrest earthquake sequence. We next
99 present the methods used in this study. We use a newly developed optical image correlation
100 technique to measure the 3D slip vectors along the 2019 Ridgecrest earthquake sequence (Fig. 1a
101 and 1b) and invert these to determine the orientation and shape of the 3D deviatoric stress tensor
102 to understand its spatial variability. We next present our results and implications. We use the
103 coseismic stress state to assess the influence of fault strength excess, the difference between the
104 critical shear stress (often referred to as the yield shear stress) needed for slip to occur and the
105 initial shear stress. We show that, as expected from theory, the more critically stressed faults
106 released a larger amount of coseismic slip (e.g., Aochi, Madariaga and Fukuyama, 2002; Kase and
107 Day, 2006). From assuming a Mohr-Coulomb failure criterion, we are then able to estimate the
108 absolute magnitude of the principal stresses as well as the static and dynamic friction coefficients.

109

110 **1.1 Tectonic setting**

111

112 The 2019 Ridgecrest earthquake sequence occurred between the transition of the 160-km wide
113 Eastern California Shear Zone (ECSZ) located to the south and the Walker Lane located to the
114 north which both accommodate northwest-trending dextral shearing of up to ~25% of the Pacific–
115 North America plate boundary motion (Dixon *et al.*, 2000; Rockwell *et al.*, 2000; McClusky *et al.*,
116 2001; Hammond and Thatcher, 2004). Both tectonic regions have hosted three major historical
117 earthquakes, including the 1873 Owens Valley earthquake located 45 km to the north of the
118 Ridgecrest rupture, and the 1992 M_w 7.3 Landers and 1999 M_w 7.1 Hector Mine events, both
119 located ~110 km to the southeast in the Mojave Desert. These events likely reflect the
120 accommodation of distributed dextral strain within the continental interior caused by the transfer
121 of Pacific-North American plate boundary motion away from the San Andreas fault, located to the
122 west, as it bends westward north of the Transverse ranges (Bennett *et al.*, 2003; Faulds, Henry and
123 Hinz, 2005; Wesnousky, 2005).

124 The unusual rupture of faults with orthogonal and mechanically unfavorable orientations
125 during the 2019 Ridgecrest earthquake sequence have been thought to arise from crustal rotation
126 caused by regional dextral simple shear strain. Such crustal rotations were observed in the current
127 interseismic crustal velocity field using GNSS (Fialko and Jin, 2021). Although there is currently
128 limited constraint of the paleoseismic history of the faults involved in the 2019 rupture sequence,
129 it is thought that they are structurally immature due to the slow velocity of the mainshock rupture
130 (Ross *et al.*, 2019; Chen *et al.*, 2020; Goldberg *et al.*, 2020; Wang *et al.*, 2020), the relatively
131 unorganized fracture pattern (Ponti *et al.*, 2019), wide zone of coseismic inelastic finite strain
132 (Antoine *et al.*, 2021; Milliner *et al.*, 2021) and relatively low cumulative displacements (0.3-1.6
133 km) (Andrew and Walker, 2020; Milliner *et al.*, 2021).

134

135 **2.0 Methods**

136

137 **2.1 Measuring 3D Surface Deformation Using Optical Image Correlation**

138

139 To measure the tectonic surface deformation pattern we use a new optical image correlation
140 technique that we have developed called COSI-Corr⁺ (Aati, Milliner and Avouac, 2022). We apply
141 this open-source and automated image processing technique for the first time to resolve the full
142 3D deformation field of the Ridgecrest earthquake sequence as this method offers a number of
143 benefits over current image matching approaches.

144

145 Standard image correlation resolves the 2D horizontal displacement with sub-pixel
146 precision typically by applying a frequency correlation scheme, which is based on the principal
147 that a translation in space is equivalent to a shift in phase in the Fourier domain (Leprince *et al.*,
148 2007; Avouac and Leprince, 2015). More recently a number of matching approaches have been
149 developed to resolve the full 3D deformation pattern (i.e., additionally measuring the vertical
150 component of surface motion) using geodetic imaging datasets. The iterative closest point
151 algorithm (ICP) is such an approach that is typically applied to pre- and post-event point clouds
152 acquired by airborne or terrestrial lidar (Besl and McKay, 1992; Nissen *et al.*, 2012). ICP solves
153 for the 3D deformation field by iteratively solving for a local rigid-body transformation (translation
154 and rotation) that minimizes the square sum of the distances between a tangential plane of a
reference point and its paired point in the target tile.

155 The most common method for solving the 3D surface deformation using optical satellite
156 or aerial images is to solve independently for the horizontal and vertical deformation components,
157 which we refer to as the ‘2+1D’ approach. Here in-track stereo image pairs are required both before
158 and after an earthquake in order to produce pre- and post-digital elevation models (DEM). The
159 pre- and post-raw images are then orthorectified with the respective DEM’s and the 2D horizontal
160 component of surface motion is determined using a standard image correlation technique. The
161 vertical component is then estimated by differencing the two DEMs which are aligned to one
162 another by accounting for the lateral translation provided by the horizontal deformation result
163 (Avouac and Leprince, 2015).

164 Although these approaches have wide use, the accuracy of the resulting deformation maps
165 can be affected by a number of factors. The ICP approach requires an estimate of the local surface
166 normal, which makes it highly sensitive to noise in the point cloud which is dependent upon the
167 DEM quality. This requires smoothing to help remove outliers that results in loss of spatial
168 resolution and details of the deformation pattern. Second, the ICP matching result may not always
169 reflect the true 3D displacement. This can occur in regions of low relief as the ICP method attempts
170 to find the closest Euclidean distance between point clouds that has no independent constraint of
171 the amount or direction of lateral translation, thereby making it susceptible to biases such as
172 apparent topography. For optical image matching techniques, both the traditional 2D and ‘2+1D’
173 approaches typically contain orthorectification, topographic, satellite jitter, sensor array and
174 aliasing artifacts that can all contaminate the final deformation result.

175 The new COSI-Corr⁺ algorithm offers several advancements that addresses some of the
176 aforementioned issues affecting current matching approaches. First, this includes optimization of
177 the rigorous sensor model (RSM), which contains information of the satellite velocities, positions,
178 attitudes and sensor orientations. Refinement of the RSM parameters is performed by optimizing
179 the locations of a set of ground control points with an orthorectified reference dataset. This
180 refinement leads to a more accurate estimate of the satellite look vector to each image pixel
181 location thereby helping reduce registration and orthorectification artifacts. Second, we have
182 implemented a ray tracing step, which is used to invert for the intersection of the various satellite
183 look directions and triangulate the 3D position of each image pixel. Knowing the 3D location of
184 each pixel from all images acquired before and after the earthquake along with the amount of
185 translation between every image pair, that is determined by the image correlation step, then allows

186 us to solve for and separate apparent surface motion caused by the 3D tectonic deformation from
187 translation caused by the parallax effect due to topography. Finally, as a post-processing step we
188 apply an independent component analysis (ICA) to the deformation maps, which is a multivariate
189 statistical technique that deconstructs a dataset into a set of statistically independent sources
190 (Gualandi, Serpelloni and Belardinelli, 2016). ICA is used to separate and isolate the tectonic
191 signal - which is a source common to all of the image correlations - from sensor artifacts, which
192 are sources associated with specific images. The new COSI-Corr⁺ technique also offers the
193 advantage in that the final deformation results are insensitive to the type or resolution of the DEM
194 used and is flexible in that it can process optical images acquired by different satellite platforms.
195 The latter is especially useful as it provides a greater number of satellite look vectors with which
196 to more accurately triangulate the 3D position of pixels. Additional processing details are
197 described in Aati et al. (2022).

198 The general COSI-Corr⁺ workflow involves five main steps, this includes 1) the RSM
199 refinement, 2) image orthorectification and resampling, 3) sub-pixel image correlation, 4) 3D
200 displacement calculation via ray tracing and 5) deconstruction of the 3D deformation maps with
201 ICA (for additional details see Aati et al., 2022). This workflow results in a final set of three
202 deformation maps where the surface motion is decomposed into the east-west, north-south and
203 vertical component of motion (see Fig. S1).

204 To measure the surface deformation field we processed 26 WorldView-1 (0.55 m pixel
205 resolution), 32 WorldView-2 (0.55 m pixel resolution), 30 WorldView-3 (0.36 m pixel resolution),
206 and two SPOT satellite images (1.5 m pixel resolution), where we used 113 orthorectified aerial
207 images (0.6 m resolution) as the reference dataset. These satellite images span a time frame
208 between 2016-2021 (see Table S1 for details). To determine the uncertainty of the deformation
209 maps we measured the surface motion in a far-field, stable region away from the coseismic
210 ruptures. Here we find the uncertainty in the east-west, north-south and vertical directions is 0.7
211 m, 0.6 m and 0.6 m at the 90% confidence level, respectively. This processing workflow results in
212 a significant reduction of topographic, orthorectification, and CCD array artifacts (with a reduction
213 of uncertainty in the deformation maps by a factor of ~3.6 compared to a result using the traditional
214 ‘2+1 D approach’), and near complete removal of aliasing artifacts associated with the SPOT 6
215 images (see Aati et al., 2022 for details).

216 To then measure the coseismic slip vectors along the rupture from the 3D deformation
217 maps we used stacked profiles orientated across the foreshock and mainshock ruptures. This allows
218 us to measure the magnitude of the total differential surface motion in the fault-parallel,
219 perpendicular, and vertical directions (see Fig. S2). This approach gives the advantage of providing
220 an estimate of the total fault offset magnitude across the rupture that is not affected by the amount
221 of distributed off-fault strain that can vary along the rupture. If distributed off-fault strain was not
222 accounted for it would lead to an underestimation of the total fault offset that would bias our
223 understanding of how stress affects the along-fault variation of the coseismic slip magnitude. The
224 coseismic slip vectors were then constructed from the total offset in the three components of
225 motion, which were measured every 138 m along the rupture across 24 different fault strands. This
226 resulted in a total of 240 slip vector measurements (see Fig. 1). The slip vectors exhibit a diverse
227 range in rake, with left-lateral slip along the foreshock rupture, right-lateral slip along the majority
228 of the mainshock rupture, and near it's northern termination we find left-lateral slip along
229 conjugate faults and oblique dextral-normal slip (see Fig. S2). Comparing the coseismic slip
230 vectors measured here with those from other studies using standard geodetic image matching
231 techniques shows very strong agreement for the horizontal component (with a correlation
232 coefficient of 0.97, see Fig. S3) (Morelan and Hernandez, 2020; Gold, DuRoss and Barnhart,
233 2021). In addition, the vertical component of slip that we measure shows good qualitative
234 agreement with that observed in field surveys. For example, regions of subsidence near the
235 northern termination of the mainshock rupture occurs along a known graben structure and
236 subsidence that we resolve along multiple right-releasing transtensional bends of the mainshock
237 rupture were also observed by field mapping surveys (Ponti *et al.*, 2019; DuRoss *et al.*, 2020).

238

239 **2.2 Coseismic Slip Vector Inversion for Stress Orientation**

240

241 To estimate the 3D deviatoric stress tensor, we invert the unit slip vectors under the
242 Wallace-Bott assumption that slip is parallel to the shear stress (Michael, 1984). The stress
243 inversion provides an estimate of the orientation and shape of the 3D deviatoric stress tensor but
244 not its magnitude. A similar approach was previously applied using field surface observations
245 following the 2010 M_w 7.1 El-Mayor Cucapah earthquake (Fletcher, Oskin and Teran, 2016). Here
246 we use measurements from optical image correlation that provides spatially dense and regular

247 measurements of slip along the entire Ridgecrest surface rupture that allows constraint of the
248 spatial variation of the stress state. The principal deviatoric stresses, σ_1 , σ_2 , σ_3 are ordered from
249 most to least compressive and the shape of the tensor is quantified from $R = [\sigma_1 - \sigma_2]/[\sigma_1 - \sigma_3]$.
250 Under a strike-slip stress regime where σ_2 is vertical, a value of $R = 0$ signifies a transtensional
251 regime, $R = 0.5$ a purely strike-slip regime and $R = 1$ a transpressional regime. To resolve spatial
252 variations of stress along the rupture we distinguish three zones from NNW-to-SSE along the
253 mainshock rupture, making sure that each contains sufficient diversity of fault orientation to
254 resolve the stress tensor. We refer to these as the northern, central, and southern zones (see Fig.
255 1a). Synthetic tests show that each of the three stress domains contain sufficient diversity in the
256 orientation of the observed slip vectors (see Fig. S4) as they can all successfully recover a known
257 stress tensor that is derived from seismicity (Hardebeck, 2020).

258 To invert the unit slip vectors for stress we use an iterative L_1 inversion because it is less
259 sensitive to outliers than a standard L_2 least squares inversion (Aster, Borchers and Thurber, 2011).
260 To minimize overfitting of the data and to constrain stress to be spatially smooth along the rupture
261 we apply a damping constraint to the inversion that penalizes large changes of the stress orientation
262 between neighboring zones (i.e., the gradients of the model vector between cells) (Hardebeck and
263 Michael, 2006). The strength of the damping factor is estimated from the fall-off of the variance
264 reduction curve because this approach is less ambiguous than a standard L-curve (Hreinsdóttir *et*
265 *al.*, 2006; Xu *et al.*, 2016). The uncertainties of the stress model are then estimated from
266 bootstrapping via random replacement of the original unit slip vectors.

267

268 **2.3 Fault Friction and Absolute Stresses from Changes in Coseismic Slip**

269

270 In our analysis we describe the relation between the fault instability (a term that
271 characterizes how close a fault is to the failure envelope), stress drop and coseismic slip magnitude
272 (see Fig. 2 for illustration of variables used). This relation assumes a Mohr-Coulomb yielding
273 criterion and constant stress drop within each of the three stress zones along the rupture ($\Delta\tau$) with
274 no cohesion that is attributed to the pre-existing nature of the ruptured fault (Thompson Jobe *et*
275 *al.*, 2020). First, the stress drop is defined by the difference between the initial (τ_o , i.e., prior to the
276 onset of seismic waves and the direct effect) and the dynamic shear stress (τ_d), which assumes the
277 stress drop is uniform within each stress domain,

278

279

$$\Delta\tau = \tau_o - \tau_d$$

280

281

$$\Delta\tau = (\mu_s - \mu_d)\sigma'_n, \quad 1$$

282

283 where μ_s is the static friction, μ_d is the dynamic friction and σ'_n is the effective normal stress

284 where the pore pressure is not specified. The effective normal stress for a fault of a given

285 orientation can be expressed as (see Fig. 2),

286

287

$$\sigma'_n = P + \Delta\sigma_c \cdot \sin(\theta_s - \phi_s), \quad 2$$

288

289 where ϕ_s is the angle of internal friction (i.e., $\arctan[\mu_s]$), and the angle θ_s is measured in

290 degrees relative to the angle corresponding to the critical failure plane ϕ_s (where $\psi = \theta_s - \phi_s$ is

291 represented in Fig. 2). $\Delta\sigma_c$ is the distance in stress space, between the stress vector corresponding

292 to the fault orientation and the center of the maximum Mohr circle. Because the intermediate

293 principal stress is vertical, P is the mean horizontal stress. If the fault plane is vertical, the stress

294 on that fault is located on the maximum Mohr circle and $\Delta\sigma_c$ is then equal to the maximum shear

295 stress $\Delta\sigma$.

296

297 The shear stress along a given fault plane, τ can be expressed as

298

299

$$\tau = \Delta\sigma_c \cdot \cos(\theta_s - \phi_s). \quad 3$$

300

301 Eq. (1) can then be re-written using eq. (2) and (3) as

302

303

$$\Delta\tau = \Delta\sigma_c \cdot \cos(\theta_s - \phi_s) - \mu_d(P + \Delta\sigma_c \cdot \sin[\theta_s - \phi_s]). \quad 4$$

304

305 P can be expressed by the following and is represented geometrically in the lower left of figure

306 2,

307

308
$$P = \frac{\Delta\sigma}{\sin(\phi_s)},$$

309

310 and from eq. (5) the stress drop can be re-written as,

311

312
$$\Delta\tau = \Delta\sigma_c \cdot \cos(\theta_s - \phi_s) - \mu_d \left[\frac{\Delta\sigma}{\sin(\phi_s)} + \Delta\sigma_c \cdot \sin(\theta_s - \phi_s) \right]. \quad 6$$

313

314 We can then re-write eq. 6 using the fault instability (I) (Vavryčuk, 2013), a term which

315 quantifies how close to failure a fault is

316

317
$$I = \frac{\tau - \mu_s(\sigma'_n - 1)}{\mu_s + \sqrt{1 + \mu_s^2}}, \quad 7$$

318

319 where the shear stress (τ) and effective normal stress (σ'_n) are calculated from the normalized stress

320 tensor and the fault orientation, and μ_s is an unknown quantity. This quantity characterizes the

321 fault's proximity to failure based on its orientation, static friction, and the stress tensor. The value

322 of I varies between 0 and 1, where higher values indicate faults that are more favorably oriented

323 for failure. We re-write the fault instability as

324

325
$$I = \frac{\lambda \cos(\theta_s) + \sin(\phi_s)}{1 + \sin(\phi_s)}, \quad 8$$

326

327 where $\lambda = \Delta\sigma_c / \Delta\sigma$ and solving for θ_s we find

328

329
$$\theta_s = \cos^{-1} \left(\frac{I + I \cdot \sin[\phi_s] - \sin[\phi_s]}{\lambda} \right). \quad 9$$

330

331 We relate the average fault slip magnitude (D) to the stress drop as a function of the downdip

332 rupture width (W), shear modulus (G) using,

333

334
$$D = \frac{W\Delta\tau}{cG}, \quad 10$$

335

336 where C which is a geometrical term of 0.59 (estimated for a strike slip fault for the central zone
 337 with length (L) of 13 km measured from our deformation maps, Fig. S1), with $(2/\pi)\sqrt{L/W}$ from
 338 Aki (1972). For the Ridgecrest rupture we assume a standard shear modulus $G = 30$ GPa that is
 339 consistent with the Southern California Earthquake Center community velocity model (Shaw *et*
 340 *al.*, 2015; Wang *et al.*, 2020) and a vertical rupture width $W = 15$ km, estimated from finite fault
 341 source models (Fig. 1c) (Wang *et al.*, 2020).

342

343 Using eq. (10) and eq. (6) we can now relate the coseismic slip magnitude to the orientation of
 344 each slip vector with respect to the stress field via

345

$$346 \quad D = \frac{W}{CG} \cdot \left(\Delta\sigma_c \cdot \cos(\theta_s - \phi_s) - \mu_d \left[\frac{\Delta\sigma}{\sin(\phi_s)} + \Delta\sigma_c \cdot \sin(\theta_s - \phi_s) \right] \right). \quad 11$$

347

348 From eq. (8) the coseismic slip magnitude can then be related to the fault instability,

349

$$350 \quad D = \frac{W}{CG} \cdot \left(\Delta\sigma_c \cdot \cos \left(\cos^{-1} \left(\frac{I + I \cdot \sin[\phi_s] - \sin[\phi_s]}{\lambda} \right) - \phi_s \right) - \mu_d \left[\frac{\Delta\sigma}{\sin\phi_s} \right. \right. \quad 12$$

$$351 \quad \left. \left. + \Delta\sigma_c \cdot \sin \left(\cos^{-1} \left(\frac{I + I \cdot \sin[\phi_s] - \sin[\phi_s]}{\lambda} \right) - \phi_s \right) \right] \right).$$

352

353 This quasi-static relation describes how the coseismic slip magnitude (D) varies depending on how
 354 optimally aligned a fault is relative to the stress field (I) and the amount of stress that is released
 355 due to the rupture. We can constrain most of the terms in eq. 12 to then estimate the frictional
 356 coefficients. As stated, W , C and G are constrained quantities, while we determine $\Delta\sigma$ from
 357 measuring temporal stress rotations that occurred after the mainshock event. Specifically, $\Delta\sigma$ is
 358 estimated by comparing the orientation of the pre-mainshock stress state (determined from our slip
 359 vector inversion) with the post-mainshock stress orientation (derived from aftershocks) using the
 360 approach of Hardebeck and Hauksson (2001) (for details see section 3.2 and section S1). In
 361 addition, as we know the geometry of the faults and the normalized stress tensor from the slip
 362 vector inversion, we can estimate I by calculating the normalized shear and normalized effective
 363 normal stresses from eq. 7. The slip magnitude, D , is measured along the rupture from our 3D
 364 surface deformation maps (see Fig. 1a, b and S1-S3). Therefore, as the only unknown quantities

365 in eq. 12 are μ_d and μ_s (where the latter is related to I using eq. 7 and ϕ_s is the angle of internal
366 friction), we can now use this relation to invert for the frictional coefficients.

367 To summarize, the relations described above assume that the magnitude of coseismic slip
368 is determined by how much the shear stress drops from an initial value (τ_o) to a dynamic one (τ_d).
369 This quasi-static approach assumes that the shear stress decreases to a constant dynamic value
370 within each of the three stress zones (but can vary between them) as it is expected that sufficient
371 sliding has occurred for the fault surface to be fully weakened and to have reached a steady-state
372 dynamic friction as is observed in laboratory experiments carried out at seismic slip rates (Di Toro
373 *et al.*, 2011). Therefore, any variations of the slip magnitude within each of the zones along the
374 rupture must then result from variations of the initial shear stress. We relate changes of the initial
375 shear stress to changes of the fault orientation with respect to the ambient stress field. For example,
376 faults that are well aligned to the stress field should have a higher initial shear stress, thereby giving
377 a larger stress drop ($\tau_o - \tau_d$) and a larger slip magnitude compared to faults that are more
378 orthogonal to σ_1 , which would exhibit tractions with lower initial shear stress, a smaller shear
379 stress change and therefore smaller slip amounts. Here we use the geometry of a restraining fault
380 bend in this sense (see Fig. 1a and b for location). This sensitivity of slip magnitude with the fault
381 orientation (and thereby the initial stresses) is what we use to constrain the frictional properties of
382 the ruptured faults. This sensitivity is introduced in our derivation above where we start from a
383 simple quasi-static shear stress change (eq. 1) to a relation that includes the effect of a fault
384 orientation that varies with the ambient stress field which acts to alter the traction on the fault
385 surface (eq. 12). We apply this relation to the slip magnitude measured along the 19° restraining
386 bend where quasi-static stress effects should be most significant.

387 From calculating μ_s using eq. 12, we can then calculate the angle of the fault (ϕ_o) at critical
388 failure relative to the direction of the maximum compressive stress via the following

389

$$390 \quad \phi_o = \frac{\pi}{4} - \frac{1}{2} \arctan(\mu_s). \quad 13$$

391

392 The initial shear stress at the point of failure (τ_o) can now be estimated by the following relation

393

$$394 \quad \tau_o = \Delta\sigma \cdot \sin(2\phi_o), \quad 14$$

395

396 and is used to estimate the effective normal stress at the point of failure (σ'_0),

397

$$398 \quad \sigma'_0 = \frac{\tau_0}{\mu_s}. \quad 15$$

399

400 The mean absolute horizontal stress (P) can now be estimated with eq. (5) or via the following,

401

$$402 \quad P = \sigma'_0 + \Delta\sigma \cdot \cos(2\phi_o). \quad 16$$

403

404 The absolute values of the principal stresses ($\sigma_i, i = 1, 2, 3$, where σ_1 is the maximum compressive
405 stress) can then be calculated following,

406

$$407 \quad \sigma_1 = P + \Delta\sigma$$

408

$$409 \quad \sigma_3 = P - \Delta\sigma, \quad 17$$

410

411 and the intermediate compressive principal stress can be found using the shape ratio (R) derived
412 from our slip vector inversion,

413

$$414 \quad \sigma_2 = \sigma_1 - R(\sigma_1 - \sigma_3). \quad 18$$

415

416 **3.0 Results**

417 **3.1 Deviatoric Stress Orientation**

418

419 From inversion of the slip vector measurements across the three stress domains, we find
420 the horizontal principal directions of the coseismic deviatoric stress tensor rotates $\sim 12^\circ$ eastward
421 from south to north along the mainshock rupture and becomes increasingly transtensional (see Fig.
422 3 d-f). Here we find R decreases from 0.45 ± 0.05 in the south to 0.28 ± 0.08 in the central region
423 and to 0.08 ± 0.06 in the north. Overall, the unit slip vectors predicted from the best-fitting stress
424 model are very close to the observed coseismic unit slip vectors (illustrated by agreement of black
425 and gray vectors in Fig. 3a-c) with a variance reduction of 96%, and a median angular misfit of 4° .

426 From measuring the relative orientation of coseismic Riedel and conjugate Riedel fractures
427 that we identified from fault traces mapped at the surface by field surveys and high-resolution
428 aerial imagery (Ponti *et al.*, 2019; Rodriguez Padilla *et al.*, 2021), we can estimate the horizontal
429 direction of the maximum compressive stress (SH_{\max}) that is independent of the SH_{\max} expected
430 by our stress model. Comparing the SH_{\max} measured from the orientation of coseismic fractures
431 with that predicted by our stress model shows a good agreement with a median angular misfit of
432 $3.7 \pm 12.5^\circ$ (see section S2 for details). This is almost a factor of three improvement compared to
433 a single-domain stress model where we would assume no spatial variability of the stress state along
434 the rupture (see Fig. S5). We also find that our stress results are robust given the number of zones
435 chosen (for $n \leq 3$) for the inversion (Fig. S5 and S6). In addition, our stress model shows a
436 remarkable agreement with the pre-seismic stress tensor derived from previous studies using
437 background seismicity (illustrated by symbols in Fig. 3 d-f) (Yang, Hauksson and Shearer, 2012;
438 Hardebeck, 2020; Sheng and Meng, 2020).

439

440 **3.2 Absolute Stress Magnitudes**

441

442 We next calculate the magnitude of the deviatoric stress (characterized using the maximum
443 shear stress $\Delta\sigma = [\sigma_1 - \sigma_3]/2$) within each zone from the rotation of the stress tensor before and
444 after the Ridgecrest earthquakes following the approach of Hardebeck and Hauksson (2001). The
445 stress rotation is estimated by comparing the stress tensor derived from our slip rake inversion,
446 which we assume characterizes the initial pre-event stress state, with the stress orientation derived
447 from aftershock focal mechanisms (Hauksson and Jones, 2020; Sheng and Meng, 2020; Wang and
448 Zhan, 2020). This assumes that the stress orientation does not vary significantly as a function of
449 depth. This assumption is supported by i) a focal mechanism inversion analysis by Duan *et al.*,
450 (2022) that found no appreciable change in the orientation with depth, and ii) the agreement of the
451 pre-earthquake background stress state estimated from other studies using seismicity at depth with
452 our own stress estimate (illustrated in Fig. 3 d-f). Differences in the pre- and post-stress states
453 show a temporal rotation of SH_{\max} after the M_w 7.1 event, which we estimate as $-5.2 \pm 1.8^\circ$, 1.3
454 $\pm 1.2^\circ$ and $7.0 \pm 1.2^\circ$ (at the 1σ level, with clockwise as positive with respect to the primary
455 ruptured faults) for the northern, central, and southern zones respectively (see Fig. 5, section S1
456 for details and Table 1). Using eq. S1 and the measured stress rotations gives $\Delta\sigma \approx 6.2$ MPa for

457 the northern zone, 9.0 MPa for the central zone (that includes the mainshock epicenter) and 2.0
458 MPa for the southern zone. To include the effects of the uncertainty of the stress tensor into the
459 estimate of the frictional coefficients, we take the distribution of SH_{\max} , that is derived from the
460 stress tensor bootstrap sample (which has a 1σ variability of $\sim 2^\circ$), and we propagate this
461 uncertainty through to get a distribution for the stress rotation, $\Delta\sigma$ and the static and dynamic
462 frictional coefficients (see Fig. S7 for the parameter distributions). We note the values of $\Delta\sigma$ are
463 in the range of previous estimates following the 1992 M_w 7.3 Landers earthquake located further
464 south in the Mojave Desert (shown by green dots in Fig. 5) and agree with a deviatoric stress
465 magnitude of 8 MPa estimated from stress rotations located near the epicenter of the M_w 7.1
466 Ridgecrest mainshock by Sheng and Meng (2020).

467 To estimate the absolute magnitude of the 3D principal stresses, the dynamic (μ_d) and static
468 friction (μ_s) we assume a Mohr-Coulomb failure criterion and given that the faults ruptured in
469 2019 were pre-existing (Thompson Jobe *et al.*, 2020) we assume that cohesion can be neglected.
470 We apply the quasi-static analysis to the central zone, as it contains the transpressional fault-bend.
471 From eq. 1-18 we find $\sigma_1 = 26.4$ MPa, $\sigma_2 = 21.2$ MPa and $\sigma_3 = 8.3$ MPa (see Table 2 for stress
472 tensor details). Given that σ_2 is vertical (fig. 3 d-f) and assuming an hydrostatic depth profile for
473 the effective normal stress (with $\rho_c = 2700$ kg/m^3 , $\rho_w = 1000$ kg/m^3), the stresses estimated
474 here are representative of the top 1.3 km of the crust ($z = \sigma_2 / [(\rho_c - \rho_w) * g]$). We note that in the
475 occurrence of pressurized fluids in the crust, our hydrostatic assumption would mean the pore
476 pressure stress profile and the representative depth (z) are underestimated. Therefore, the
477 representative depth (z) should be considered as a lower bound estimate (i.e., the shallowest
478 possible depth) in the occurrence of pressurized fluids in the crust.

479

480 **3.3 Static and Dynamic Fault Friction**

481

482 The slip tapering along the central bend of the main rupture occurs far from the southern end of
483 the fault, where the rupture propagated for another 15 km along the southern segment beyond the
484 bend. We therefore consider that the varying fault strike is the main cause of the tapering of slip
485 along the transpressional bend. To test this hypothesis and understand its implications for fault
486 friction we use the theoretical relation we derived between fault slip and fault instability (eq. 12)
487 to solve for μ_s and μ_d . We determine the best-fitting values of $\mu_s = 0.61 \pm 0.14$ and μ_d to $0.29 \pm$

488 0.04 (black and blue line in Fig. 6a, respectively) with the uncertainty estimated from a random
489 replacement bootstrapping of the slip data. This variation of the slip magnitude as a function of
490 the fault instability provides an excellent fit to the observations with a variance reduction of
491 98.14%, which captures the gradual decrease of slip magnitude with decreasing fault instability
492 (red line in Fig. 6d). Interestingly, the location of the fault at the epicenter in Mohr space (shown
493 as the star in Figure 6a) is located very close to the failure envelope. This gives a stress drop at the
494 failure point of 4.04 ± 0.49 MPa (shown by blue downward arrow in Fig. 6a).

495 Given the stresses and friction now resolved along the rupture, we can compare how the
496 coseismic slip magnitude varies as a function of the normalized normal and shear stress projected
497 onto the fault. At each point along the rupture where we have an estimate of fault slip, we calculate
498 the fault instability, I , as defined by equations 7 and 8 (Vavryčuk, Bouchaala and Fischer, 2013;
499 Vavryčuk, 2014). The fault instability and slip magnitude are both highest at the epicenter ($I > 0.9$
500 and slip = 4-5 m) and both decrease southwards along the 19° bend of the primary rupture (Fig. 6
501 b and c). Specifically, along the restraining bend the coseismic slip magnitude linearly decreases
502 by as much as ~2.5 m, from ~3.8 m north of the bend to ~1.2 m south of it (see Fig. 1b). Similarly,
503 we find the fault becomes more misorientated to the stress field from north-to-south along the bend
504 (where SH_{\max} is ~N7°E), which is shown by a 27% decrease of the fault instability from ~0.95
505 north of the bend to ~0.68 south of it (see Fig. 1b, 6 b, c and 7a).

506 The estimate of the dynamic friction ($\mu_d = 0.29 \pm 0.04$) agrees within the uncertainty but
507 is slightly lower than an upper bound estimate of $\mu_d = 0.33$ derived from the state of stress on the
508 fault segment with the lowest observed fault instability (black dashed line Fig. 6a). Lastly, the
509 static friction value that we invert for using the slip data ($\mu_s = 0.61 \pm 0.14$) is at the upper end of
510 a prior estimate of $\mu_s = 0.4-0.6$ made by Fialko (2021) who used a different approach based on the
511 dihedral angles of conjugate faults in the host rock surrounding the 2019 Ridgecrest rupture using
512 seismicity lineations.

513 In Mohr stress space the relation of slip magnitude and fault instability is illustrated by
514 larger slip values located closer to the failure envelope (where I is maximum at the failure
515 envelope, Fig. 6a). As a fault plane is located further away from the failure envelope and becomes
516 increasingly mis-aligned to the stress field (i.e., I decreases), the slip magnitude measured within
517 the central zone is found to gradually taper (red-white colored circles in Fig. 6a), which is
518 associated with a ~10 MPa increase of the normal stresses and ~1.5 MPa decrease of the shear

519 stresses. Alternatively, this can be seen in the stereographs where higher slip is limited to the higher
520 fault instability regions (Fig. 3 a-c). We note that this comparison includes slip vectors only along
521 the primary rupture strands and excludes points along shorter, parallel secondary faults, as the slip
522 magnitude is expected to be limited by fault length. The northern zone is also consistent with this
523 behavior of higher slip closer to the failure envelope and a decrease in magnitude away from it,
524 but the northward tapering of slip could also be affected by the rupture termination (see Fig. S8).
525 Following our quasi-static assumption (eq. 12) we inverted the coseismic slip (D) for friction for
526 both the central and southern zones (the northern zone lacks a sufficient range of slip magnitude
527 to obtain robust values). Here we find appreciable differences in the frictional properties between
528 the two stress zones (Fig. 7a). To explain the observed slip magnitude in the southern zone and its
529 variability given it occurred in a region of the crust with a lower maximum shear stress magnitude
530 of $\Delta\sigma = 2.01$ MPa compared to the central zone ($\Delta\sigma = 9.01$ MPa, which are values determined
531 from the stress rotations, see Table 1), the dynamic friction within the southern zone must have
532 been significantly lower at $\mu_d = 0.10 \pm 0.04$ compared to the central zone ($\mu_d = 0.29 \pm 0.04$).
533 However, we note that the variability in the slip magnitude within the southern zone could also be
534 affected by dynamic stresses associated with the rupture termination that are not considered by our
535 quasi-static assumption here. This is one reason why our analysis is focused on the central stress
536 zone that is located away from the fault terminations and on the effect of a prominent 19°
537 transpressional fault bend where the effect of quasi-static stresses are expected to be largest.

538

539

540 **4.0 Discussion**

541 **4.1 How Heterogenous Are Stresses in the Crust?**

542 We conclude first that the assumption of a uniform stress field at the scale of the central
543 zone (~ 13 km in length) can explain relatively well the tapering of slip (a decrease of ~ 2.5 m)
544 along a 19° transpressional fault bend as it increases the effective normal stress and decreases the
545 shear stress. This interpretation is in contrast with the suggestion that the slip tapering could have
546 resulted from heterogeneities of static stress changes induced by the foreshock rupture (Chen *et*
547 *al.*, 2020; Lozos and Harris, 2020; Zhang *et al.*, 2020; Cortez *et al.*, 2021). The data show however
548 some scatter around the model prediction which can reflect such heterogeneities of the initial
549 stress. The scatter must also reflect the uncertainties on the measurements of the fault orientation

550 and slip and heterogeneities of dynamic friction. Inertial effects during the rupture would also
551 result in departure from the model prediction since equation 12 assumes a quasistatic rupture
552 process. Disentangling the various sources of misfits is therefore not straightforward.
553 Heterogeneities of the stress field are however at least required when we compare the stress tensors
554 derived for the three zones considered in our stress inversion. So, while stress heterogeneities must
555 exist, they seem to play a subsidiary role in explaining the 2.5 m decrease in slip magnitude
556 observed along the prominent rupture bend.

557 The stress orientation and its spatial variability is a key initial condition for physics-based
558 numerical models to accurately simulate dynamic ruptures and the resulting strong ground motion
559 (Olsen *et al.*, 2009; Graves *et al.*, 2011). Our inversion for the coseismic stress shows two features
560 that change from south to north along the mainshock rupture. First, a 12° rotation of SH_{\max} and the
561 second, a ~50% decrease of the stress ratio indicating an increasingly transtensional stress regime
562 in the direction towards the Basin and Range province. Both of these features are in strong
563 agreement with the background pre-stress determined from pre-Ridgecrest focal mechanism
564 seismicity (Hardebeck, 2020; Hauksson *et al.*, 2020; Sheng and Meng, 2020; Wang and Zhan,
565 2020). Additional evidence to support the notion of a spatial variability in the stress field is that
566 from south to north along the mainshock rupture the fault strike rotates eastward and becomes
567 increasingly northward orientated which mimics the along-strike rotation of SH_{\max} . This change of
568 the general fault strike may be a result of it adjusting over geologic timescales to become more
569 optimally aligned to the change in SH_{\max} direction.

570 Here we conclude that the background stresses inferred from seismicity provide a
571 reasonable estimate of the initial stresses and that they can explain the first-order observed
572 variability of coseismic slip along the rupture length (Fig. 7). A forward calculation of the pre-
573 mainshock stress state given by focal mechanism inversion of seismicity over the period before
574 the 2019 Ridgecrest sequence (Hardebeck, 2020), shows it can explain a significant amount of the
575 observed variability of the coseismic slip orientation along both the foreshock and mainshock
576 ruptures (with a 92% variance reduction and a median angular difference of 6.77 ± 7.3 , see Fig.
577 S9, which is similar to our best fitting stress model with a variance reduction of 95%, see Fig. 7b).
578 A close correspondence of the shear traction direction derived from the background stress with the
579 coseismic slip rake was also found at seismogenic depths from estimates provided by a kinematic
580 slip inversion of geodetic and seismologic data for the 2016 M_w 7.1 Kumamoto earthquake in

581 Japan (Matsumoto *et al.*, 2018). These results support the notion that *a priori* knowledge of the
582 background stress and fault geometry can provide a reasonable constraint of the expected variation
583 in the direction of coseismic slip (i.e. the rake) along a given fault system at the first-order, 5-10
584 km scale (while assuming no stress perturbations from other processes) (Fig. 7b).

585

586 **4.2 Fault Friction of Developing Faults Systems**

587

588 The frictional resistance of faults is an important mechanical property that determines the
589 level of shear stress faults can sustain. As faults are thought to structural evolve over time through
590 strain localization and smoothing of the fault surface as they accumulate slip, the friction is thought
591 to weaken (i.e., the level of shear stress that can be sustained is reduced) as different weakening
592 mechanisms may start to take effect (Rice, 2006; Sagy, Brodsky and Axen, 2007; Noda, Dunham
593 and Rice, 2009; Renard, Mair and Gundersen, 2012; Collettini *et al.*, 2019). The frictional strength
594 of the faults that ruptured during the 2019 Ridgecrest earthquake sequence exhibit a strong
595 Byerlee-type static strength ($\mu_s = 0.61 \pm 0.14$). Such a strong friction might not be surprising for
596 an intra-crustal and immature fault system. An intermediate-strong frictional strength ($\mu_s = 0.4$ -
597 0.6) was however found by Fialko (2021) for smaller faults in the region surrounding the 2019
598 Ridgecrest earthquake sequence. A mechanism that was proposed to explain the lower frictional
599 values is that long-term crustal tectonic rotation has progressively misaligned these relatively
600 young faults to the ambient stress field, which in turn has weakened them and would indicate a
601 frictional regime that is undergoing transition from an initially strong (e.g., $\mu_s = 0.60$) to a weak
602 shear strength (Fialko, 2021; Fialko and Jin, 2021). The static friction we estimate here supports
603 the notion of a classical static strength for an intra-crustal fault that is early in its structural and
604 frictional development.

605 However, unlike immature faults, there is still debate regarding the frictional strength of
606 mature plate-boundary fault systems. Specifically, whether mature faults are weak and sliding
607 occurs at shear stresses well below the failure envelope predicted by Byerlee's law. The lack of a
608 heat flow anomaly across the San Andreas fault and its possible mis-orientation to the background
609 stress field have been proposed as evidence for mature faults having low frictional strength (Brune,
610 Henyey and Roy, 1969; Lachenbruch and Sass, 1980; Zoback *et al.*, 1987; Rice, 1992; Scholz,
611 2000; Hardebeck and Michael, 2004). Although future work could address this still debated

612 question by applying the stress and friction analysis outlined here to forthcoming ruptures along
613 mature fault systems, we envision it will be challenging to do so. The primary issue is that most
614 mature fault systems have far simpler fault geometries closer to planar than immature faults. This
615 would make it difficult to detect strong quasi-static stress effects induced by large geometrical
616 changes such as fault bends, as these are needed to alter the normal and shear stresses and cause
617 the required variation of slip (D) as a function of I to invert for the frictional parameters (eq. 12).

618 Lastly, we note that the stress change effects from the foreshock on the mainshock rupture
619 segments are estimated to be small in the area of the fault bend that we are analyzing in this study
620 and are unlikely to explain the decrease in coseismic slip along the fault bend (Lozos & Harris,
621 2020). The displacement points that we used in our frictional analysis are located away from the
622 foreshock-mainshock junction, where stress changes are largest. The normal and shear stress
623 effects in the near-surface are estimated to be $<0.5\text{MPa}$ along the bend that we analysis (Lozos &
624 Harris, 2020). If we were to account for the small difference in these stress changes induced by
625 the foreshock, this would have the effect of translating points in the Mohr space by a small amount
626 (i.e., that in Fig. 6a) and therefore would have a small effect on the frictional coefficient estimate.

627

628 **4.3 Effect of Initial Stresses on Rupture Propagation**

629

630 The unusually slow rupture of the mainshock was a notable feature of the M_w 7.1 mainshock event.
631 Various mechanisms have been proposed to explain the ~ 2 km/s rupture velocity including, a
632 geometrically complex fault system (Goldberg *et al.*, 2020) or stress unloading due to the M_w 6.4
633 foreshock (Chen *et al.*, 2020). Dynamic rupture simulations have shown that fault bends can also
634 affect the rupture velocity as the change in fault geometry alters the static initial stresses applied
635 to the fault surface. It has been found for example, that restraining bends larger than 10° can
636 decelerate the rupture substantially due to the locally larger initial normal stress (Kase and Day,
637 2006). More specific to the M_w 7.1 Ridgecrest earthquake, results from dynamic rupture modeling
638 of Zhang *et al.* (2020) confirms a ‘stress barrier’ effect due to high initial normal and low shear
639 static stresses along the same fault bend that we study. Here our results are consistent with a change
640 of the stresses projected onto the fault due to the variation of the fault’s geometry along-strike. Our
641 best fitting stress tensor shows that the 19° change in the fault orientation brought this rupture
642 segment further away from an optimal alignment and closer to a perpendicular one with respect to

643 the σ_1 direction ($\sim N7E^\circ$). This had the effect of decreasing the degree of optimal fault alignment
644 by $\sim 27\%$ (Fig. 6b and d) and as we argue from our quasi-static analysis resulted in a ~ 2.5 m
645 decrease of coseismic slip (Fig. 6c and 7a). Thus, our results support the occurrence of a significant
646 increase in the initial normal stresses along the fault bend, which as expected from theoretical
647 simulations, could have contributed to the unusually slow rupture propagation southwards and
648 away from the mainshock epicenter.

649 Our analysis shows 1) that the initial shear stress along the fault bend seems primarily
650 affected by the local fault strike (rather than spatial heterogeneities of the ambient stress field in
651 the surrounding crust along the rupture at length scales < 10 km), 2) that the slip rake is dictated
652 by the pre-seismic shear stress direction and 3) that the slip amplitude is dictated by the drop of
653 initial shear stress to a uniform dynamic friction. We estimate $\mu_d = 0.29 \pm 0.04$ a value which is
654 within the 0.05-0.4 range of steady-state dynamic friction measured in laboratory experiments at
655 seismic slip rates on dry rocks (~ 1 m/s) (Di Toro *et al.*, 2011). The value of the fault instability for
656 which the predicted slip is null according to our model provides an estimate of the maximum
657 possible mis-orientation that would allow rupture propagation under quasi-static conditions. For
658 $\mu_d = 0.29$ it means the orientation of reactivated faults must have an azimuth in the range between
659 $\sim 8^\circ$ and 66° from σ_1 (i.e., the range of ϕ limited by μ_d in fig. 6a) and that the magnitude of slip
660 quickly diminishes as the fault orientation diverges from
661 $\sim 30^\circ$ (as shown in fig. 6 a and d and according to eq. 12). Fault misorientation was however not
662 a key factor in arresting the rupture during the Ridgecrest mainshock. There are however examples
663 of seismic ruptures that terminated where the fault becomes highly mis-oriented to the surrounding
664 stress field. This includes the southern termination of the 1999 M_w 7.1 Hector Mine rupture
665 (Hauksson, Jones and Hutton, 2002) and the northern end of the 1992 M_w 7.3 Landers earthquake
666 (Wollherr, Gabriel and Mai, 2019)). In the case of the Landers earthquake, the rupture seems to
667 have jumped from faults that became gradually misoriented to more optimally oriented faults
668 leading to a highly segmented rupture (Bouchon, 1997).

669 The close correlation of coseismic slip magnitude with fault instability (Fig. 6d) that is
670 explained by our quasi-static model, shows that the slip magnitude and rake orientation could be
671 estimated *a priori* by assuming a standard value of the static and dynamic friction, as well as the
672 background stress orientation, deviatoric stress magnitude (or maximum shear stress) and the fault
673 geometry (e.g., Fig. 7). However, along-fault slip variability has also been seen from other events

674 and geomorphic analysis to correlate with the lateral fault segmentation, with local slip tapering
675 on segments and slip troughs in inter-segment areas (Manighetti *et al.*, 2005; Klinger, Michel and
676 King, 2006; Elliott, Dolan and Oglesby, 2009; Klinger, 2010; Rockwell and Klinger, 2013;
677 Milliner *et al.*, 2016). Such observations suggest that changes in fault orientation and stress that
678 we show here are not the only mechanism to explain slip tapering along fault segments, which
679 could also include variations in material properties, stress perturbations from prior ruptures, fault
680 structural maturity and dynamic stresses amongst other effects (Bürgmann, Pollard and Martel,
681 1994; Dieterich and Smith, 2010; Dunham *et al.*, 2011; Perrin *et al.*, 2016). Dynamic rupture
682 simulations of the seismic cycle are however still needed to fully assess the effect of fault
683 segmentation and fault termination.

684

685 **5.0 Conclusions**

686

687 Using a new 3D optical image correlation technique we have been able to capture the variations
688 of the coseismic slip orientation and magnitude along a surface rupture at the hundreds of meters
689 scale. These coseismic slip measurements can be explained by spatial variations of the stress field
690 at the ten's of kilometer scale along the mainshock rupture, that is consistent with the known
691 background stress state. From our analysis we show that for most of the rupture, co-seismic fault
692 slip, is determined by the magnitude of the maximum shear stress in the surrounding crust ($\Delta\sigma$),
693 the angle of the fault relative to the direction of the driving stress (characterized by the fault
694 instability, I) and how much the frictional resistance of the fault surface decreases during sliding
695 (i.e., the difference between μ_s and μ_d). By deriving a relation between these quantities and
696 measuring them, where D is estimated from the surface deformation maps, $\Delta\sigma$ is measured from
697 temporal stress rotations, and I is calculated from the known fault geometry and the normalized
698 stress tensor (where the latter is itself determined from inverting the coseismic slip vectors), we
699 are then able to invert for the static and dynamic frictional strength of the ruptured faults. We find
700 the faults that ruptured are statically strong ($\mu_s = 0.61 \pm 0.14$) but dynamically weaken ($\mu_d =$
701 0.29 ± 0.04). We note that this relationship holds only along fault segments where quasi-static
702 stresses are larger than the dynamic stresses generated at the rupture tip, which is expected along
703 large geometrical fault changes such as bends. We find this effect of the varying fault orientation
704 with respect to the applied stress regime on the coseismic slip magnitude is consistent with

705 theoretical predictions (Aochi, Madariaga and Fukuyama, 2002; Kase and Day, 2006). The
706 frictional analysis outlined here, opens up the possibility to constrain the absolute stress
707 magnitudes and understand the degree of frictional strength and weakening that can occur during
708 surface rupturing events along other fault systems with curved geometries exceeding 10's of
709 degrees.

710

711

712 **Open Research**

713 Optical Images were made available through NASA NGA commercial archive data service
714 (<https://cad4nasa.gsfc.nasa.gov/index.php>, which is provided under the NextView license
715 agreement. Maps were made using Generic Mapping Tools ([https://www.generic-mapping-
716 tools.org/](https://www.generic-mapping-tools.org/)). The COSI-Corr image correlation software can be accessed from
717 (http://www.tectonics.caltech.edu/slip_history/spot_coseis/download_software.html). The
718 measurements of the coseismic fault slip vectors, the 3D displacement maps and the MATLAB
719 scripts to invert the coseismic slip vectors for the deviatoric stress tensor can be found from the
720 Zenodo open repository <https://doi.org/10.5281/zenodo.7162335>.

721

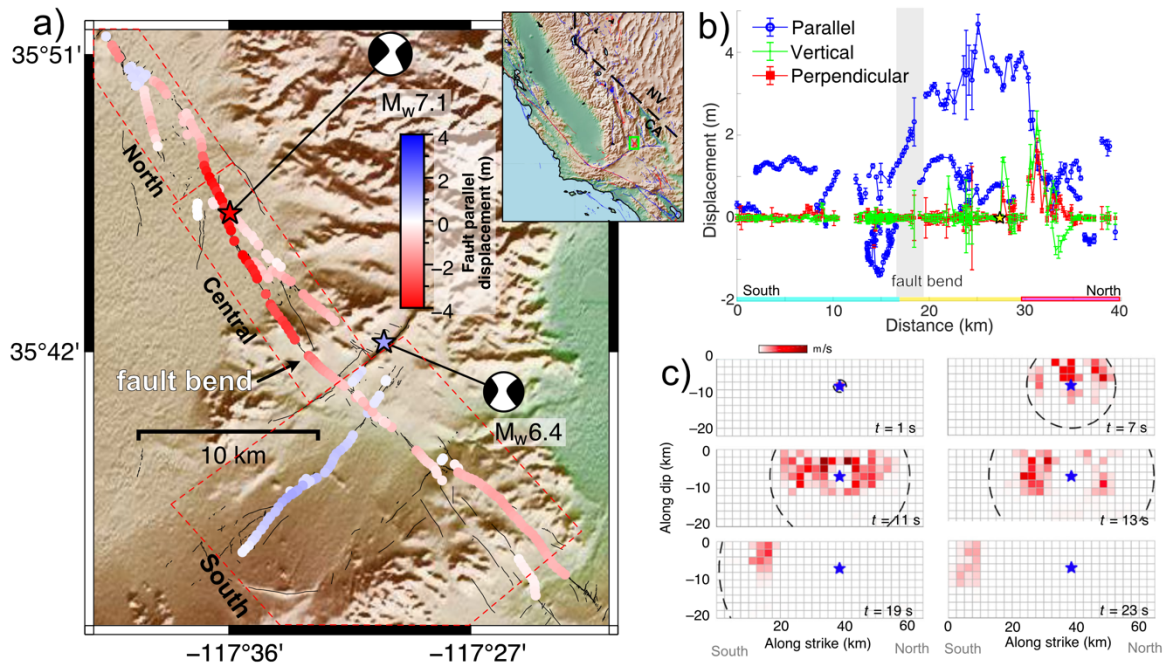
722

723 **Acknowledgements**

724 We thank Jeanne Hardebeck, Xin Wang, Egill Hauksson and Shuzhong Sheng for making their
725 stress results available. We thank Kim Olson, the editor Isabelle Manighetti, the associate editor
726 and two anonymous reviewers for their comments and suggestions which helped strengthen the
727 manuscript. We thank the NASA NGA commercial archive data service for access to the World
728 View imagery (<https://cad4nasa.gsfc.nasa.gov/index.php>) which is provided under the NextView
729 license agreement. **Funding:** This research was supported by the NASA Earth Surface and Interior
730 focus area and performed at the Jet Propulsion Laboratory, California Institute of Technology
731 (80NM0018D0004). Satellite imagery for this project were also purchased under SCEC grant
732 #19222. **Author contributions:** All authors contributed to this study and participated in
733 manuscript preparation. **Competing interests:** The authors declare that they have no competing
734 interests.

735

736



737

738 **Figure 1. Coseismic slip vectors and rupture kinematics.** (a) fault-parallel component of slip

739 measured from optical image correlation. Red dashed boxes correspond to the three stress zones.

740 b) Slip distribution illustrating the fault-parallel (blue, where negative denotes left-lateral slip),

741 perpendicular (red) and vertical (green) along the direction of the mainshock surface rupture

742 measured from the 3D deformation maps (see Fig. S1), star shows epicenter location. Cyan, yellow

743 and magenta horizontal bars at bottom denote the extent of the southern, central and northern

744 zones, respectively. Change of fault strike associated with rupture bend is denoted by vertical gray

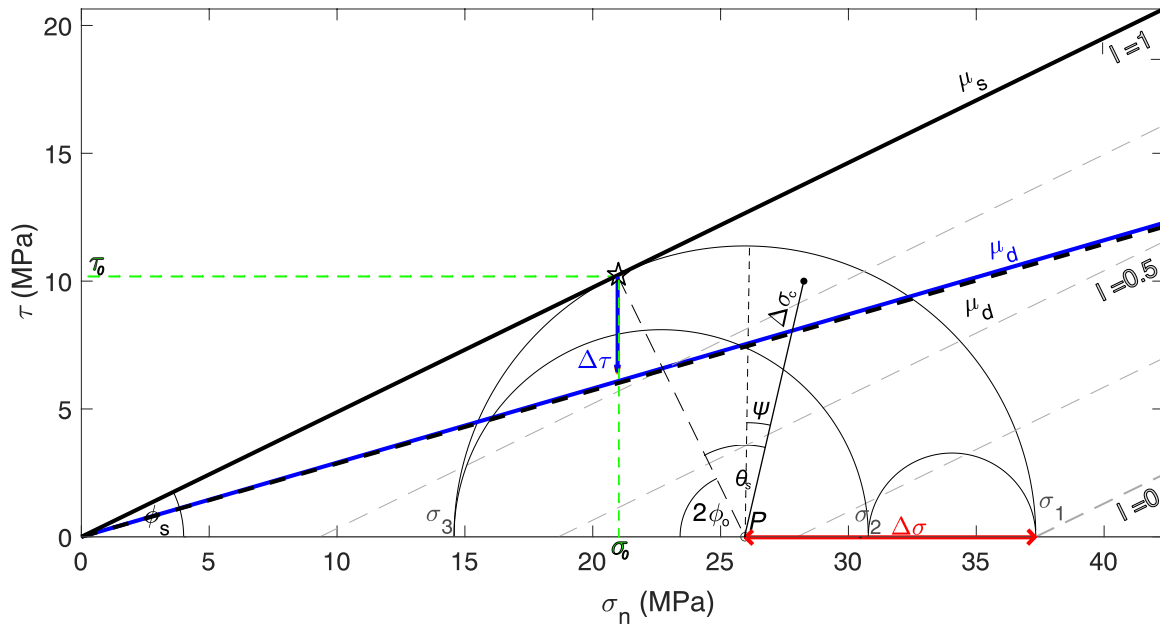
745 bar. c) Rupture kinematics of the $M_w 7.1$ mainshock constrained by inversion of seismic and

746 geodetic data, which illustrates the transition from initial crack-like to pulse-like rupture, viewing

747 southwest, panel adapted from (Chen *et al.*, 2020).

748

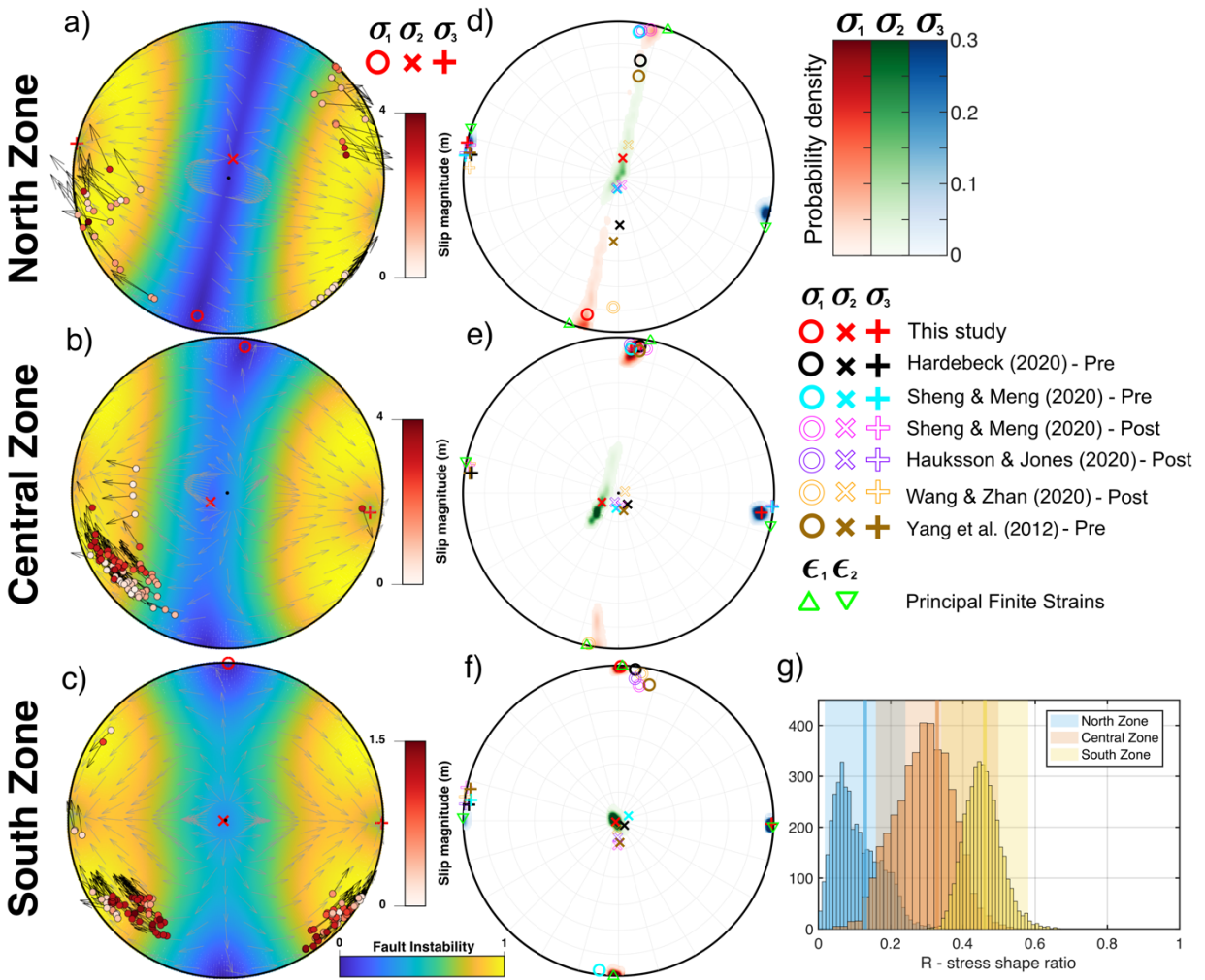
749



750

751 Figure 2. Mohr circle illustrating the variables used in equations 1-18. Black filled circle shows
 752 the location in Mohr space of the state of stress on a plane with an arbitrary orientation. Effective
 753 normal stress is positive in compression (with values shown here only for illustrative purposes),
 754 and for illustration purposes positive shear stresses are parallel to dextral motion. Black solid line
 755 denotes the static friction (μ_s), black dashed and blue lines are dynamic friction (μ_d) estimated
 756 from the observed slip vector with lowest fault instability (I , gray lines) giving an upper bound to
 757 μ_d , and that inverted from our slip-fault instability model (red line in Figure 5d). Absolute
 758 stresses are estimated with knowledge of the maximum shear stress ($\Delta\sigma$) and mean horizontal
 759 stress (P). Internal angle of friction is ϕ_s , the angle between the failure plane and maximum
 760 principal stress (σ_1) is denoted by ϕ_o , the angle or deviation of an arbitrary failure plane (black
 761 dot) from the optimal angle with the failure envelope is shown by θ_s , with $\Delta\sigma_c$ denoting the
 762 stress differential from P that accounts for fault planes located away from the Mohr circle, the
 763 stress drop is shown by $\Delta\tau$, normal and shear stress on the critical failure plane is shown by
 764 σ_o and τ_o , respectively. The angle $\psi = \theta_s - \phi_s$.

765



766

767

768 **Figure 3. Stress state derived from inversion of coseismic slip vectors.** a-c) show lower-

769 hemisphere stress stereographs of the three stress zones, a) is northern zone, b) central zone and c)

770 southern zone) with the color background showing the fault instability (see eq. 7 and 8) and light

771 gray vectors showing the predicted slip direction given by the stress model. Black vectors show

772 the observed slip vectors where red-white colored dots denote the slip magnitude. d-f) show lower-

773 hemisphere projection stereonets of the 3D stress tensor from our inversion (red symbols) with the

774 uncertainties (colored regions) and other stress results from inverting background and postseismic

775 seismicity (see key in top right). Finite principal strains (green triangles) are estimated from the

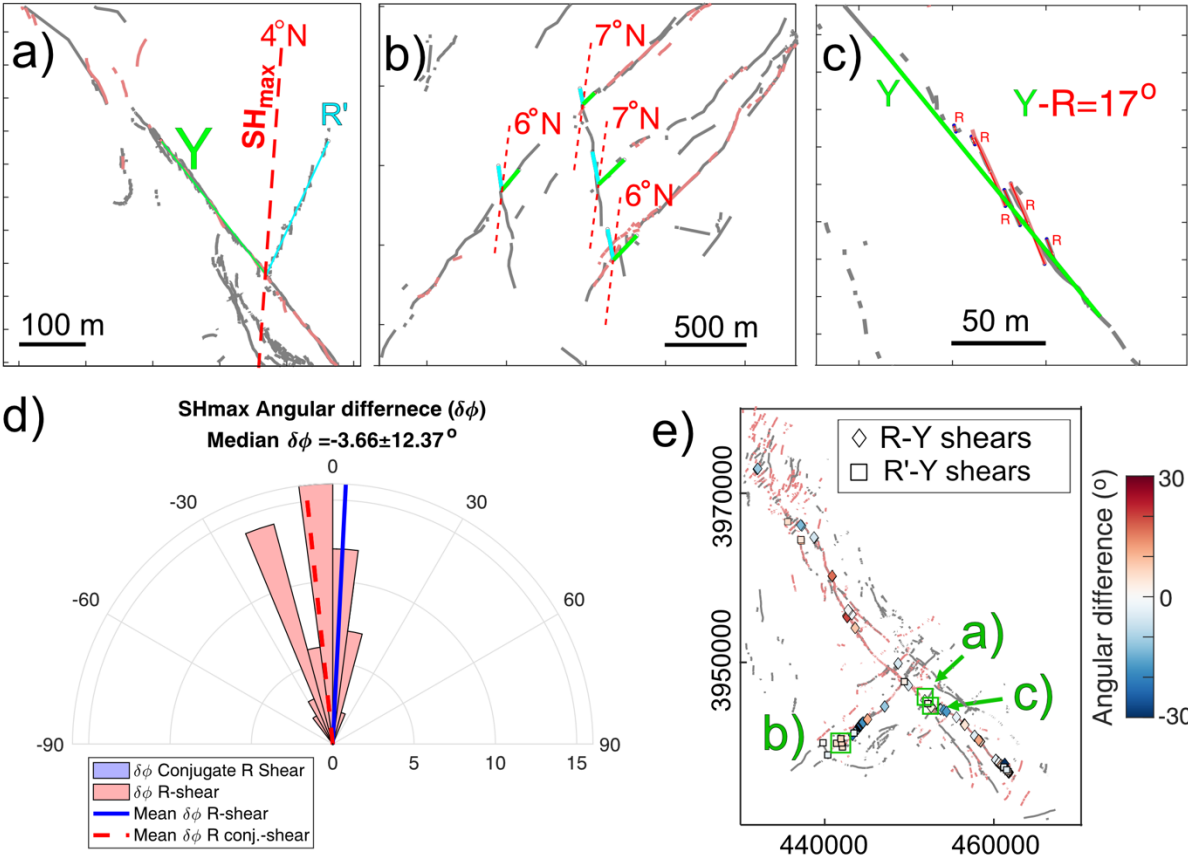
776 optical displacement maps following approach of (Milliner *et al.*, 2021). g) Distribution of R for

777 the three zones, lower values indicate an increasingly transtensional stress regime. The vertical

778 thick colored lines and transparent regions represent the mean R value and its 95% confidence
779 interval for the background stress from (Hardebeck, 2020) for the three stress zones.

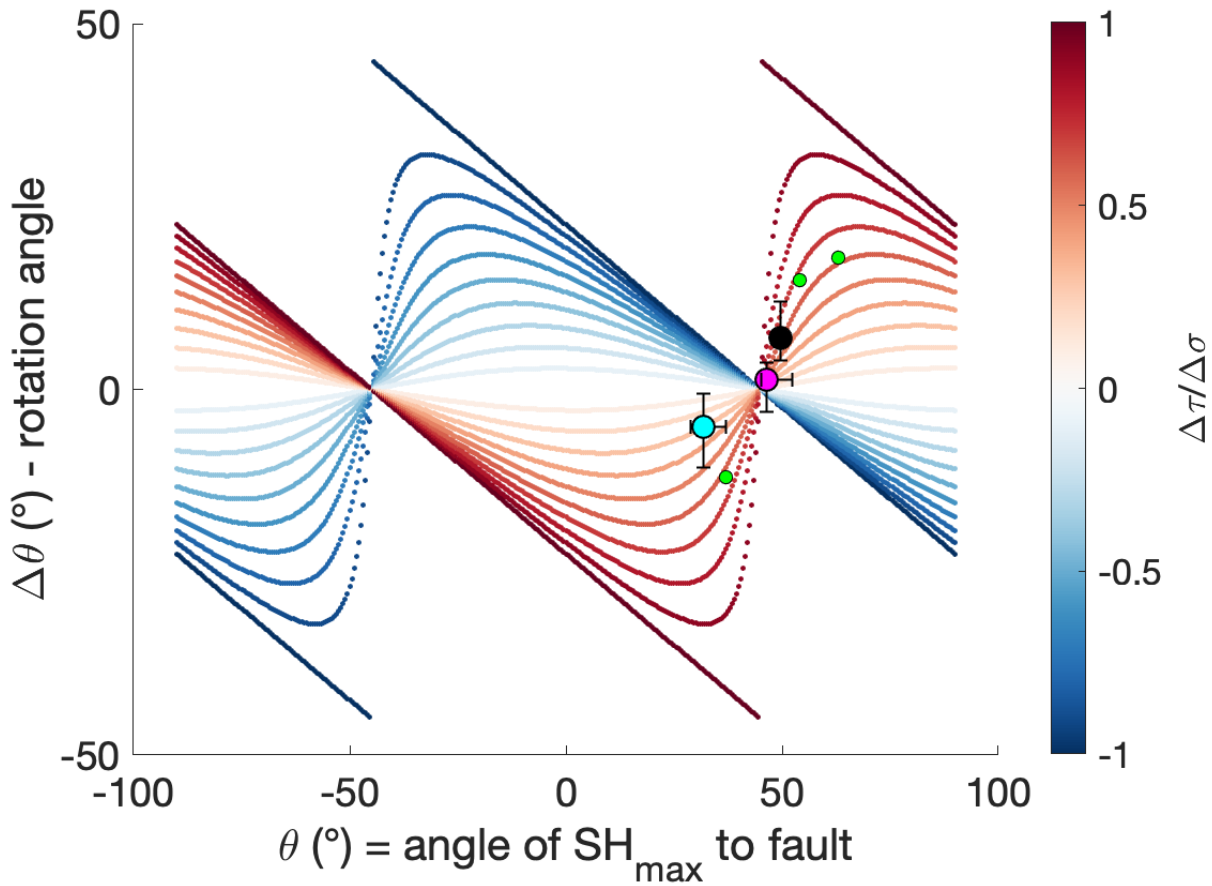
780

781



782
 783
 784
 785
 786
 787
 788
 789
 790
 791
 792
 793
 794
 795
 796
 797

Figure 4. Validation of our stress model by comparison of SH_{max} measured from coseismic surface fractures. a) Map view of an example of conjugate Riedel surface fractures (cyan lines) with through-going Y-shears (green) used to measure SH_{max} (dashed red line) along the southern portion of the mainshock rupture. Gray fault traces are from Ponti et al. (2020) and red from Rodriguez Padilla et al. (2022). b) Map view of conjugate Riedel surface fractures (cyan lines) with through-going Y-shears (green) used to measure SH_{max} (dashed red line) along the southern portion of the foreshock rupture. c) view of an example of Riedel surface fractures (red lines) with through-going Y-shears (green) used to measure SH_{max} along the southern portion of the mainshock rupture. Angle between Y-R shears shown in red. d) Polar histogram of the overall angular difference between SH_{max} from our three-zone stress model with that measured from surface fractures (where R-Y fractures are shown in red and Y-R' fractures shown in blue). e) Map view shows location and magnitude of angular difference between SH_{max} from our three-zone stress model with that measured from surface fractures (where R-Y fractures are shown in diamonds and Y-R' fractures plotted as squares).

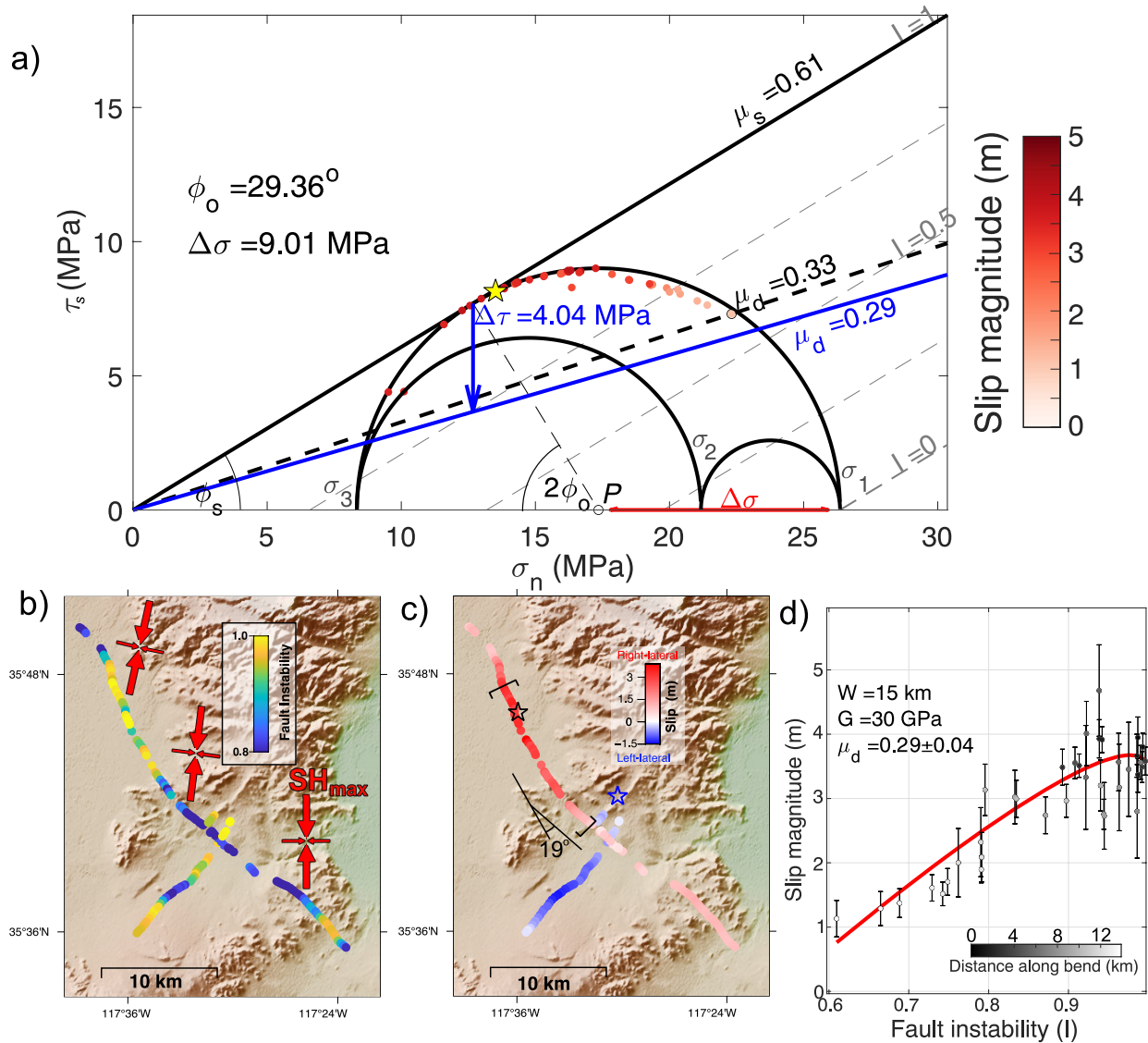


799

800 **Figure 5. Estimate of absolute magnitude of maximum shear stresses.** Cyan, magenta and
 801 black circles show the values for the north, central and southern stress zones, respectively, showing
 802 95% confidence intervals. Small green circles show the values for the segments that ruptured
 803 during the 1992 M_w 7.3 Landers rupture from (Hardebeck and Hauksson, 2001). Ratio of the stress
 804 drop ($\Delta\tau$) to the the maximum shear stress ($\Delta\sigma$) are plotted as smaller circles with red-blue color
 805 scale.

806

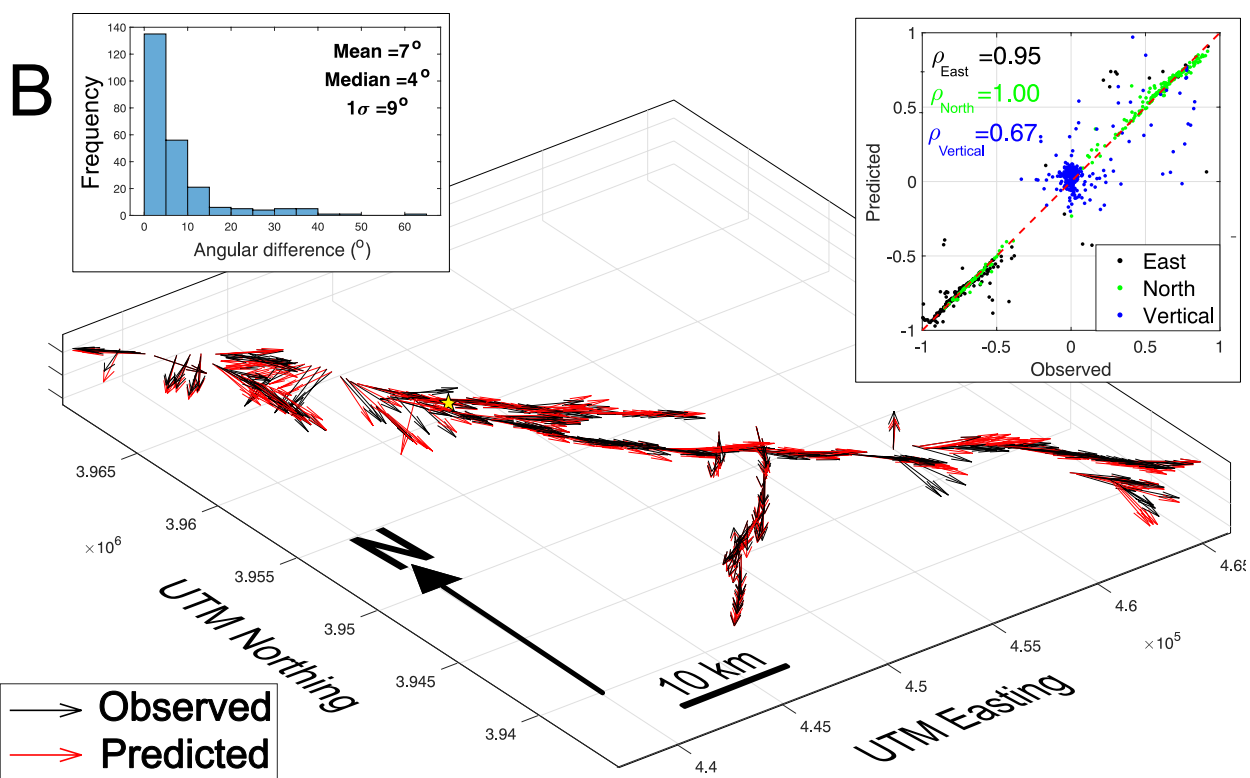
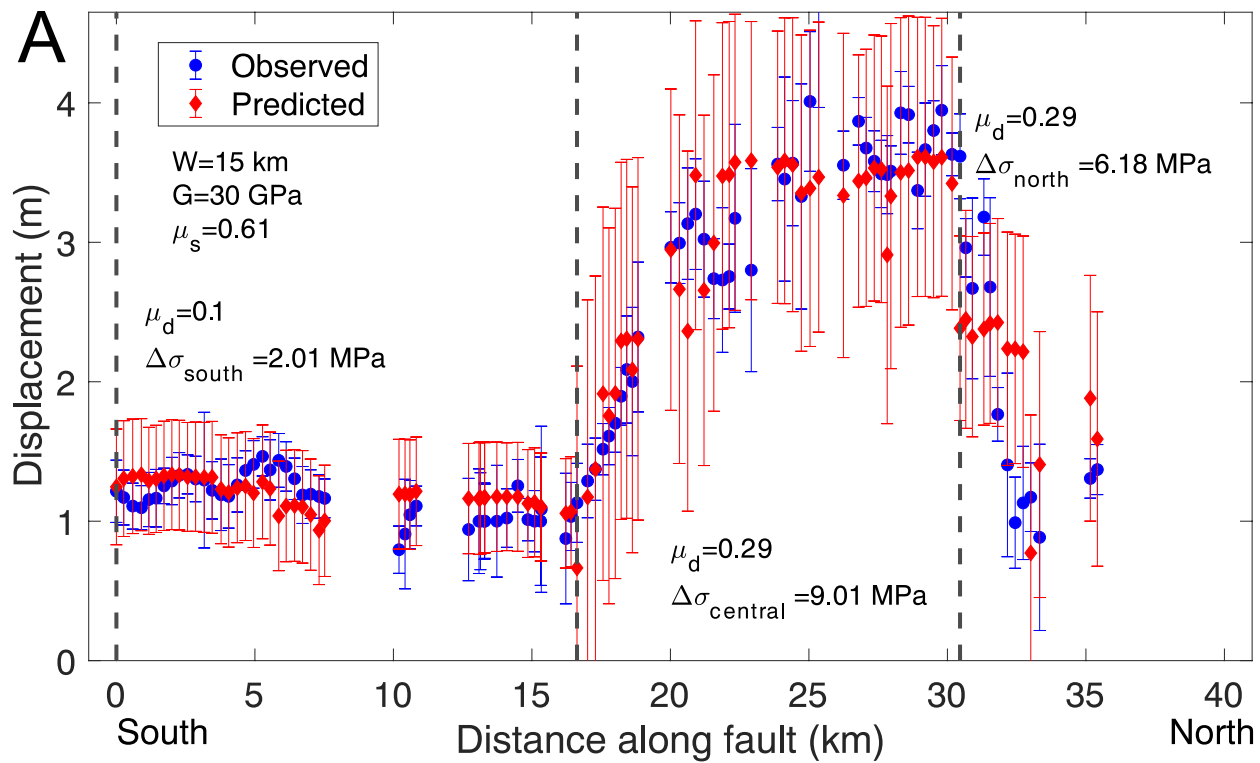
807



808

809 **Figure 6. Relation between slip and fault instability.** a) Slip vectors in Mohr space of the central
 810 zone that contains the large-scale fault bend, with colors depicting the coseismic slip magnitude.
 811 Star shows the slip vector at the M_w 7.1 epicenter. Diagonal gray dashed lines show the fault
 812 instability (I), which decreases away from the failure envelope (Vavryčuk, 2014). b) illustrates
 813 variation of fault instability calculated from our best-fit 3D stress tensor (Fig. 2 d-f) which shows
 814 a marked southwards decrease away from the M_w 7.1 mainshock epicenter, large red arrows denote
 815 SH_{max} . c) illustrates similar southward decrease of the observed coseismic slip magnitude (shown
 816 by red dots, note blue dots are also slip magnitude but with negative sign for left-lateral slip). Bend
 817 geometry of 19° is also illustrated and brackets along mainshock rupture show points used in
 818 friction inversion shown in a) and d). d) Relation of I with observed slip magnitude along the

819 central segments of the mainshock rupture with our best-fitting slip-fault instability model (red
820 line, that is defined by eq. 12) giving a dynamic friction of 0.29 ± 0.04 (illustrated as blue line in
821 a, with uncertainty determined from 4000 bootstrap simulations of the data). Gray colorscale
822 represents the distance of a point along the restraining bend, where 0 km denotes the most
823 northwestern point along the mainshock rupture. This shows how both slip and I decrease from
824 north-to-south along the fault bend.



827 Figure 7. Comparison of the coseismic slip magnitude observed from image correlation with the
828 predicted amount from our stress model (top) and the unit slip vector orientations (bottom) a)
829 Coseismic slip profile along the mainshock rupture, viewing west, which compares geodetically
830 observed coseismic slip magnitude (blue) with our quasi-static stress model prediction (red).
831 Extent of the southern, central and northern stress zones are denoted by the black vertical dashed
832 lines (see also Fig. 1a for map view). Parameters for all three zones are shown in top left (where
833 W = seismogenic width, G = shear modulus, μ_s = static friction), while the dynamic friction (μ_d)
834 and the maximum shear stress ($\Delta\sigma$) are inverted separately for each stress domain (except the
835 northern zone due to lack of data). b) Upper left inset shows histogram of the angular difference
836 in the slip rake between the observed and predicted slip vector for the best fitting three-zone stress
837 model. Upper right inset is a correlation plot between the east-west (black dots), north-south (green
838 dots) and vertical (blue dots) components of the unit slip vectors used in the stress inversion,
839 labelled with the Pearson correlation coefficient (ρ) of each slip component. Bottom shows oblique
840 map view comparing the observed 3D unit surface slip vectors (black) measured from the 3D
841 image correlation result with those predicted (red vectors) from our best fitting stress model (also
842 illustrated by stereographs in Fig. 2 a-c), epicenter location is shown by yellow pentagram.
843
844

845 **Tables**

846 **Table 1.** Parameters used for estimating maximum shear stress ($\Delta\sigma$).

Stress zone	Pre-SHmax orientation - this study (°)	Post SHmax (°) - Hauksson & Jones (2020)	Post SHmax (°) - Sheng and Meng (2020)	Post SHmax (°) - Wang & Zhan (2020)	Average Post-SHmax (°)	Stress rotation (°)†	Avg fault strike (°)	Avg. fault displacement (m)	$\Delta\sigma$ (MPa)
North	12.9 ± 1.8	8.72	12.3	2.23	7.75	-5.15	161	1.5	6.18
Central	7.56 ± 1.2	4.54	10.86	11.17	8.86	1.3	141.6	3.5	9.01
South	1.30 ± 1.2	6.89	8.9	9.23	8.34	7.04	131.73	1	2.01

847 † = positive values are clockwise rotations

848

849 **Table 2.** Values here include the stress tensor orientation in polar co-ordinates and absolute
 850 magnitudes, the stress shape ratio (R), and the static (μ_s) and dynamic friction (μ_d). Note that the
 851 first value of N denotes the number of slip vectors used in the inversion for stress (e.g., Fig. 2),
 852 while the second denotes the number of slip vectors used in the inversion for friction (eq. 12, Fig.
 853 6). The latter are fewer because only slip along primary faults are used. Reported uncertainties are
 854 at the 1σ level.

855

Zone	N (stress/f riction)	σ_1		σ_2		σ_3		R	μ_s	μ_d
		Tr/Pl (°)	MPa	Tr/Pl (°)	MPa	Tr/Pl (°)	MPa			
North	46/-	192.8 /10.0	22.0 ±2.5	13.0/80.0	21.2±2.5	282.8/0.1	9.7 ±2.5	0.08 ±0.06	-	-
Central	80/40	6.9/5.9	26.4 ±2.5	241.1/80.0	21.2±2.5	97.8/8.1	8.3 ±2.5	0.28 ±0.08	0.61 ± 0.14	0.29 ± 0.04
South	114/45	1.0/0.2	23.1 ±2.5	259.2/88.9	21.2±2.5	91.0/1.1	19.0 ±2.5	0.45 ±0.05	-	0.10 ±0.04

856

857

858

859

860 **References**

861

862 Aati, S., Milliner, C. and Avouac, J.-P. (2022) ‘A new approach for 2-D and 3-D precise
863 measurements of ground deformation from optimized registration and correlation of optical
864 images and ICA-based filtering of image geometry artifacts’, *Remote Sensing of*
865 *Environment*, 277, p. 113038. Available at: <https://doi.org/10.1016/j.rse.2022.113038>.

866 Andrew, J.E. and Walker, J.D. (2020) ‘Total Slip Estimates of the M7.1 (July 2019) Seismogenic
867 Airport Lake Fault System, Ridgecrest, California’. *2020 GSA Annual meeting*.

868 Antoine, S.L. *et al.* (2021) ‘Diffuse Deformation and Surface Faulting Distribution from Submetric
869 Image Correlation along the 2019 Ridgecrest, California, Ruptures’, *Bulletin of the*
870 *Seismological Society of America* [Preprint]. Available at:
871 <https://doi.org/10.1785/0120210036>.

872 Aochi, H., Madariaga, R. and Fukuyama, E. (2002) ‘Effect of normal stress during rupture
873 propagation along nonplanar faults’, *Journal of Geophysical Research: Solid Earth*,
874 107(B2), p. ESE 5-1-ESE 5-10. Available at: <https://doi.org/10.1029/2001JB000500>.

875 Aster, R.C., Borchers, B. and Thurber, C.H. (2011) *Parameter Estimation and Inverse Problems*.
876 Academic Press.

877 Avouac, J.P. and Leprince, S. (2015) ‘Geodetic Imaging Using Optical Systems’, *Geodesy*, pp.
878 387–424. Available at: <https://doi.org/10.1016/B978-0-444-53802-4.00067-1>.

879 Barnhart, W.D., Hayes, G.P. and Gold, R.D. (2019) ‘The July 2019 Ridgecrest, California,
880 Earthquake Sequence: Kinematics of Slip and Stressing in Cross-Fault Ruptures’,
881 *Geophysical Research Letters*, 46(21), pp. 11859–11867. Available at:
882 <https://doi.org/10.1029/2019GL084741>.

883 Bennett, R.A. *et al.* (2003) ‘Contemporary strain rates in the northern Basin and Range province
884 from GPS data’, *Tectonics*, 22(2). Available at: <https://doi.org/10.1029/2001TC001355>.

885 Besl, P.J. and McKay, N.D. (1992) ‘A method for registration of 3-D shapes’, *IEEE Transactions*
886 *on Pattern Analysis and Machine Intelligence*, 14(2), pp. 239–256. Available at:
887 <https://doi.org/10.1109/34.121791>.

888 Bouchon, M. (1997) ‘The state of stress on some faults of the San Andreas System as inferred
889 from near-field strong motion data’, *Journal of Geophysical Research: Solid Earth*,
890 102(B6), pp. 11731–11744. Available at: <https://doi.org/10.1029/97JB00623>.

891 Brune, J.N., Henyey, T.L. and Roy, R.F. (1969) ‘Heat flow, stress, and rate of slip along the San
892 Andreas Fault, California’, *Journal of Geophysical Research (1896-1977)*, 74(15), pp.
893 3821–3827. Available at: <https://doi.org/10.1029/JB074i015p03821>.

894 Bürgmann, R., Pollard, D.D. and Martel, S.J. (1994) ‘Slip distributions on faults: effects of stress
895 gradients, inelastic deformation, heterogeneous host-rock stiffness, and fault interaction’,
896 *Journal of Structural Geology*, 16(12), pp. 1675–1690. Available at:
897 [https://doi.org/10.1016/0191-8141\(94\)90134-1](https://doi.org/10.1016/0191-8141(94)90134-1).

898 Byerlee, J. (1978) ‘Friction of Rocks’, in J.D. Byerlee and M. Wyss (eds) *Rock Friction and*
899 *Earthquake Prediction*. Basel: Birkhäuser Basel (Contributions to Current Research in
900 Geophysics (CCRG)), pp. 615–626. Available at: [https://doi.org/10.1007/978-3-0348-](https://doi.org/10.1007/978-3-0348-7182-2_4)
901 [7182-2_4](https://doi.org/10.1007/978-3-0348-7182-2_4).

902 Chen, K. *et al.* (2020) ‘Cascading and pulse-like ruptures during the 2019 Ridgecrest earthquakes
903 in the Eastern California Shear Zone’, *Nature Communications*, 11(1), p. 22. Available at:
904 <https://doi.org/10.1038/s41467-019-13750-w>.

905 Collettini, C. *et al.* (2019) ‘Beyond Byerlee friction, weak faults and implications for slip
906 behavior’, *Earth and Planetary Science Letters*, 519, pp. 245–263. Available at:
907 <https://doi.org/10.1016/j.epsl.2019.05.011>.

908 Cortez, J.T. *et al.* (2021) ‘On the Rupture Propagation of the 2019 M6.4 Searles Valley, California,
909 Earthquake, and the Lack of Immediate Triggering of the M7.1 Ridgecrest Earthquake’,
910 *Geophysical Research Letters*, 48(4), p. e2020GL090659. Available at:
911 <https://doi.org/10.1029/2020GL090659>.

912 Di Toro, G. *et al.* (2011) ‘Fault lubrication during earthquakes’, *Nature*, 471(7339), pp. 494–498.
913 Available at: <https://doi.org/10.1038/nature09838>.

914 Dieterich, J.H. and Smith, D.E. (2010) ‘Nonplanar Faults: Mechanics of Slip and Off-fault
915 Damage’, in Y. Ben-Zion and C. Sammis (eds) *Mechanics, Structure and Evolution of*
916 *Fault Zones*. Basel: Birkhäuser (Pageoph Topical Volumes), pp. 1799–1815. Available at:
917 https://doi.org/10.1007/978-3-0346-0138-2_12.

918 Dixon, T.H. *et al.* (2000) ‘Present-day motion of the Sierra Nevada block and some tectonic
919 implications for the Basin and Range province, North American Cordillera’, *Tectonics*,
920 19(1), pp. 1–24. Available at: <https://doi.org/10.1029/1998TC001088>.

921 Duan, H. *et al.* (2022) ‘Analysis of coseismic slip distributions and stress variations of the 2019
922 Mw 6.4 and 7.1 earthquakes in Ridgecrest, California’, *Tectonophysics*, 831, p. 229343.
923 Available at: <https://doi.org/10.1016/j.tecto.2022.229343>.

924 Dunham, E.M. *et al.* (2011) ‘Earthquake Ruptures with Strongly Rate-Weakening Friction and
925 Off-Fault Plasticity, Part 2: Nonplanar Faults’, *Bulletin of the Seismological Society of
926 America*, 101(5), pp. 2308–2322. Available at: <https://doi.org/10.1785/0120100076>.

927 DuRoss, C.B. *et al.* (2020) ‘Surface Displacement Distributions for the July 2019 Ridgecrest,
928 California, Earthquake Ruptures’, *Bulletin of the Seismological Society of America*, 110(4),
929 pp. 1400–1418. Available at: <https://doi.org/10.1785/0120200058>.

930 Elliott, A.J., Dolan, J.F. and Oglesby, D.D. (2009) ‘Evidence from coseismic slip gradients for
931 dynamic control on rupture propagation and arrest through stepovers’, *Journal of
932 Geophysical Research: Solid Earth*, 114(B2). Available at:
933 <https://doi.org/10.1029/2008JB005969>.

934 Faulds, J.E., Henry, C.D. and Hinz, N.H. (2005) ‘Kinematics of the northern Walker Lane: An
935 incipient transform fault along the Pacific–North American plate boundary’, *Geology*,
936 33(6), pp. 505–508. Available at: <https://doi.org/10.1130/G21274.1>.

937 Fialko, Y. (2021) ‘Estimation of Absolute Stress in the Hypocentral Region of the 2019 Ridgecrest,
938 California, Earthquakes’, *Journal of Geophysical Research: Solid Earth*, 126(7), p.
939 e2021JB022000. Available at: <https://doi.org/10.1029/2021JB022000>.

940 Fialko, Y. and Jin, Z. (2021) ‘Simple shear origin of the cross-faults ruptured in the 2019
941 Ridgecrest earthquake sequence’, *Nature Geoscience*, 14(7), pp. 513–518. Available at:
942 <https://doi.org/10.1038/s41561-021-00758-5>.

943 Fletcher, J.M., Oskin, M.E. and Teran, O.J. (2016) ‘The role of a keystone fault in triggering the
944 complex El Mayor–Cucapah earthquake rupture’, *Nature Geoscience*, 9(4), pp. 303–307.
945 Available at: <https://doi.org/10.1038/ngeo2660>.

946 Gold, R.D., DuRoss, C.B. and Barnhart, W.D. (2021) ‘Coseismic Surface Displacement in the
947 2019 Ridgecrest Earthquakes: Comparison of Field Measurements and Optical Image
948 Correlation Results’, *Geochemistry, Geophysics, Geosystems*, 22(3), p. e2020GC009326.
949 Available at: <https://doi.org/10.1029/2020GC009326>.

950 Goldberg, D.E. *et al.* (2020) ‘Complex Rupture of an Immature Fault Zone: A Simultaneous
951 Kinematic Model of the 2019 Ridgecrest, CA Earthquakes’, *Geophysical Research Letters*,
952 47(3), p. e2019GL086382. Available at: <https://doi.org/10.1029/2019GL086382>.

953 Graves, R. *et al.* (2011) ‘CyberShake: A Physics-Based Seismic Hazard Model for Southern
954 California’, *Pure and Applied Geophysics*, 168(3), pp. 367–381. Available at:
955 <https://doi.org/10.1007/s00024-010-0161-6>.

956 Gualandi, A., Serpelloni, E. and Belardinelli, M.E. (2016) ‘Blind source separation problem in
957 GPS time series’, *Journal of Geodesy*, 90(4), pp. 323–341. Available at:
958 <https://doi.org/10.1007/s00190-015-0875-4>.

959 Hammond, W.C. and Thatcher, W. (2004) ‘Contemporary tectonic deformation of the Basin and
960 Range province, western United States: 10 years of observation with the Global Positioning
961 System’, *Journal of Geophysical Research: Solid Earth*, 109(B8). Available at:
962 <https://doi.org/10.1029/2003JB002746>.

963 Hardebeck, J.L. (2020) ‘A Stress-Similarity Triggering Model for Aftershocks of the Mw 6.4 and
964 7.1 Ridgecrest Earthquakes’, *Bulletin of the Seismological Society of America*, 110(4), pp.
965 1716–1727. Available at: <https://doi.org/10.1785/0120200015>.

966 Hardebeck, J.L. and Hauksson, E. (2001) ‘Crustal stress field in southern California and its
967 implications for fault mechanics’, *Journal of Geophysical Research: Solid Earth*, 106(B10),
968 pp. 21859–21882. Available at: <https://doi.org/10.1029/2001JB000292>.

969 Hardebeck, J.L. and Michael, A.J. (2004) ‘Stress orientations at intermediate angles to the San
970 Andreas Fault, California’, *Journal of Geophysical Research: Solid Earth*, 109(B11).
971 Available at: <https://doi.org/10.1029/2004JB003239>.

972 Hardebeck, J.L. and Michael, A.J. (2006) ‘Damped regional-scale stress inversions: Methodology
973 and examples for southern California and the Coalinga aftershock sequence’, *Journal of*
974 *Geophysical Research: Solid Earth*, 111(B11). Available at:
975 <https://doi.org/10.1029/2005JB004144>.

976 Harris, R.A. and Day, S.M. (1999) ‘Dynamic 3D simulations of earthquakes on En Echelon
977 Faults’, *Geophysical Research Letters*, 26(14), pp. 2089–2092. Available at:
978 <https://doi.org/10.1029/1999GL900377>.

979 Hauksson, E. *et al.* (2020) ‘Caltech/USGS Southern California Seismic Network (SCSN) and
980 Southern California Earthquake Data Center (SCEDC): Data Availability for the 2019

981 Ridgecrest Sequence’, *Seismological Research Letters*, 91(4), pp. 1961–1970. Available at:
982 <https://doi.org/10.1785/0220190290>.

983 Hauksson, E. and Jones, L.M. (2020) ‘Seismicity, Stress State, and Style of Faulting of the
984 Ridgecrest-Coso Region from the 1930s to 2019: Seismotectonics of an Evolving Plate
985 Boundary Segment’, *Bulletin of the Seismological Society of America*, 110(4), pp. 1457–
986 1473. Available at: <https://doi.org/10.1785/0120200051>.

987 Hauksson, E., Jones, L.M. and Hutton, K. (2002) ‘The 1999 Mw 7.1 Hector Mine, California,
988 Earthquake Sequence: Complex Conjugate Strike-Slip Faulting’, *Bulletin of the
989 Seismological Society of America*, 92(4), pp. 1154–1170. Available at:
990 <https://doi.org/10.1785/0120000920>.

991 Hreinsdóttir, S. *et al.* (2006) ‘Coseismic deformation of the 2002 Denali Fault earthquake: Insights
992 from GPS measurements’, *Journal of Geophysical Research: Solid Earth*, 111(B3).
993 Available at: <https://doi.org/10.1029/2005JB003676>.

994 Kase, Y. and Day, S.M. (2006) ‘Spontaneous rupture processes on a bending fault’, *Geophysical
995 Research Letters*, 33(10). Available at: <https://doi.org/10.1029/2006GL025870>.

996 Klinger, Y. (2010) ‘Relation between continental strike-slip earthquake segmentation and
997 thickness of the crust’, *Journal of Geophysical Research: Solid Earth*, 115(B7). Available
998 at: <https://doi.org/10.1029/2009JB006550>.

999 Klinger, Y., Michel, R. and King, G.C.P. (2006) ‘Evidence for an earthquake barrier model from
1000 Mw~7.8 Kokoxili (Tibet) earthquake slip-distribution’, *Earth and Planetary Science
1001 Letters*, 242(3), pp. 354–364. Available at: <https://doi.org/10.1016/j.epsl.2005.12.003>.

1002 Lachenbruch, A.H. and Sass, J.H. (1980) ‘Heat flow and energetics of the San Andreas Fault
1003 Zone’, *Journal of Geophysical Research: Solid Earth*, 85(B11), pp. 6185–6222. Available
1004 at: <https://doi.org/10.1029/JB085iB11p06185>.

1005 Leprince, S. *et al.* (2007) ‘Co-Registration of Optically Sensed Images and Correlation (COSI-
1006 Corr): an operational methodology for ground deformation measurements’, in *2007 IEEE
1007 International Geoscience and Remote Sensing Symposium. 2007 IEEE International
1008 Geoscience and Remote Sensing Symposium*, pp. 1943–1946. Available at:
1009 <https://doi.org/10.1109/IGARSS.2007.4423207>.

1010 Lozos, J.C. and Harris, R.A. (2020) ‘Dynamic Rupture Simulations of the M6.4 and M7.1 July
1011 2019 Ridgecrest, California, Earthquakes’, *Geophysical Research Letters*, 47(7), p.
1012 e2019GL086020. Available at: <https://doi.org/10.1029/2019GL086020>.

1013 Manighetti, I. *et al.* (2005) ‘Evidence for self-similar, triangular slip distributions on earthquakes:
1014 Implications for earthquake and fault mechanics’, *Journal of Geophysical Research: Solid
1015 Earth*, 110(B5). Available at: <https://doi.org/10.1029/2004JB003174>.

1016 Matsumoto, S. *et al.* (2018) ‘Prestate of Stress and Fault Behavior During the 2016 Kumamoto
1017 Earthquake (M7.3)’, *Geophysical Research Letters*, 45(2), pp. 637–645. Available at:
1018 <https://doi.org/10.1002/2017GL075725>.

1019 McClusky, S.C. *et al.* (2001) ‘Present day kinematics of the Eastern California Shear Zone from a
1020 geodetically constrained block model’, *Geophysical Research Letters*, 28(17), pp. 3369–
1021 3372. Available at: <https://doi.org/10.1029/2001GL013091>.

1022 Michael, A.J. (1984) ‘Determination of stress from slip data: Faults and folds’, *Journal of
1023 Geophysical Research: Solid Earth*, 89(B13), pp. 11517–11526. Available at:
1024 <https://doi.org/10.1029/JB089iB13p11517>.

1025 Milliner, C. *et al.* (2021) ‘Bookshelf Kinematics and the Effect of Dilatation on Fault Zone
1026 Inelastic Deformation: Examples From Optical Image Correlation Measurements of the
1027 2019 Ridgecrest Earthquake Sequence’, *Journal of Geophysical Research: Solid Earth*,
1028 126(3), p. e2020JB020551. Available at: <https://doi.org/10.1029/2020JB020551>.

1029 Milliner, C. and Donnellan, A. (2020) ‘Using Daily Observations from Planet Labs Satellite
1030 Imagery to Separate the Surface Deformation between the 4 July Mw 6.4 Foreshock and 5
1031 July Mw 7.1 Mainshock during the 2019 Ridgecrest Earthquake Sequence’, *Seismological
1032 Research Letters*, 91(4), pp. 1986–1997. Available at: <https://doi.org/10.1785/0220190271>.

1033 Milliner, C.W.D. *et al.* (2016) ‘Resolving Fine-Scale Heterogeneity of Co-seismic Slip and the
1034 Relation to Fault Structure’, *Scientific Reports*, 6(1), p. 27201. Available at:
1035 <https://doi.org/10.1038/srep27201>.

1036 Morelan, A.E. and Hernandez, J.L. (2020) ‘Increasing Postearthquake Field Mapping Efficiency
1037 with Optical Image Correlation’, *Bulletin of the Seismological Society of America*, 110(4),
1038 pp. 1419–1426. Available at: <https://doi.org/10.1785/0120200034>.

1039 Nissen, E. *et al.* (2012) ‘Three-dimensional surface displacements and rotations from differencing
1040 pre- and post-earthquake LiDAR point clouds’, *Geophysical Research Letters*, 39(16).
1041 Available at: <https://doi.org/10.1029/2012GL052460>.

1042 Noda, H., Dunham, E.M. and Rice, J.R. (2009) ‘Earthquake ruptures with thermal weakening and
1043 the operation of major faults at low overall stress levels’, *Journal of Geophysical Research:*
1044 *Solid Earth*, 114(B7). Available at: <https://doi.org/10.1029/2008JB006143>.

1045 Olsen, K.B. *et al.* (2009) ‘ShakeOut-D: Ground motion estimates using an ensemble of large
1046 earthquakes on the southern San Andreas fault with spontaneous rupture propagation’,
1047 *Geophysical Research Letters*, 36(4). Available at: <https://doi.org/10.1029/2008GL036832>.

1048 Perrin, C. *et al.* (2016) ‘Location of largest earthquake slip and fast rupture controlled by along-
1049 strike change in fault structural maturity due to fault growth’, *Journal of Geophysical*
1050 *Research: Solid Earth*, 121(5), pp. 3666–3685. Available at:
1051 <https://doi.org/10.1002/2015JB012671>.

1052 Ponti, D.J. *et al.* (2019) ‘Digital datasets documenting surface fault rupture and ground
1053 deformation features produced by the Ridgecrest M6.4 and M7.1 earthquake sequence of
1054 July 4 and 5, 2019’, *U.S. Geological Survey Data Release* [Preprint]. Available at:
1055 <https://doi.org/10.5066/P9BZ5IJ9>.

1056 Renard, F., Mair, K. and Gundersen, O. (2012) ‘Surface roughness evolution on experimentally
1057 simulated faults’, *Journal of Structural Geology*, 45, pp. 101–112. Available at:
1058 <https://doi.org/10.1016/j.jsg.2012.03.009>.

1059 Rice, J.R. (1992) ‘Chapter 20 Fault Stress States, Pore Pressure Distributions, and the Weakness
1060 of the San Andreas Fault’, in B. Evans and T. Wong (eds) *International Geophysics*.
1061 Academic Press (Fault Mechanics and Transport Properties of Rocks), pp. 475–503.
1062 Available at: [https://doi.org/10.1016/S0074-6142\(08\)62835-1](https://doi.org/10.1016/S0074-6142(08)62835-1).

1063 Rice, J.R. (2006) ‘Heating and weakening of faults during earthquake slip’, *Journal of Geophysical*
1064 *Research: Solid Earth*, 111(B5). Available at: <https://doi.org/10.1029/2005JB004006>.

1065 Rockwell, T.K. *et al.* (2000) ‘Paleoseismology of the Johnson Valley, Kickapoo, and Homestead
1066 Valley Faults: Clustering of Earthquakes in the Eastern California Shear Zone’, *Bulletin of*
1067 *the Seismological Society of America*, 90(5), pp. 1200–1236. Available at:
1068 <https://doi.org/10.1785/0119990023>.

1069 Rockwell, T.K. and Klinger, Y. (2013) ‘Surface Rupture and Slip Distribution of the 1940 Imperial
1070 Valley Earthquake, Imperial Fault, Southern California: Implications for Rupture
1071 Segmentation and Dynamics’, *Bulletin of the Seismological Society of America*, 103(2A),
1072 pp. 629–640. Available at: <https://doi.org/10.1785/0120120192>.

1073 Rodriguez Padilla, A.M. *et al.* (2021) ‘Near-Field High-Resolution Maps of the Ridgecrest
1074 Earthquakes from Aerial Imagery’, *Seismological Research Letters*, 93(1), pp. 494–499.
1075 Available at: <https://doi.org/10.1785/0220210234>.

1076 Ross, Z.E. *et al.* (2019) ‘Hierarchical interlocked orthogonal faulting in the 2019 Ridgecrest
1077 earthquake sequence’, *Science*, 366(6463), pp. 346–351. Available at:
1078 <https://doi.org/10.1126/science.aaz0109>.

1079 Sagy, A., Brodsky, E.E. and Axen, G.J. (2007) ‘Evolution of fault-surface roughness with slip’,
1080 *Geology*, 35(3), pp. 283–286. Available at: <https://doi.org/10.1130/G23235A.1>.

1081 Scholz, C.H. (2000) ‘Evidence for a strong San Andreas fault’, *Geology*, 28(2), pp. 163–166.
1082 Available at: [https://doi.org/10.1130/0091-7613\(2000\)28<163:EFASSA>2.0.CO;2](https://doi.org/10.1130/0091-7613(2000)28<163:EFASSA>2.0.CO;2).

1083 Shaw, J.H. *et al.* (2015) ‘Unified Structural Representation of the southern California crust and
1084 upper mantle’, *Earth and Planetary Science Letters*, 415, pp. 1–15. Available at:
1085 <https://doi.org/10.1016/j.epsl.2015.01.016>.

1086 Sheng, S. and Meng, L. (2020) ‘Stress Field Variation During the 2019 Ridgecrest Earthquake
1087 Sequence’, *Geophysical Research Letters*, 47(15), p. e2020GL087722. Available at:
1088 <https://doi.org/10.1029/2020GL087722>.

1089 Thompson Jobe, J.A. *et al.* (2020) ‘Evidence of Previous Faulting along the 2019 Ridgecrest,
1090 California, Earthquake Ruptures’, *Bulletin of the Seismological Society of America*, 110(4),
1091 pp. 1427–1456. Available at: <https://doi.org/10.1785/0120200041>.

1092 Vavryčuk, V. (2014) ‘Iterative joint inversion for stress and fault orientations from focal
1093 mechanisms’, *Geophysical Journal International*, 199(1), pp. 69–77. Available at:
1094 <https://doi.org/10.1093/gji/ggu224>.

1095 Vavryčuk, V., Bouchaala, F. and Fischer, T. (2013) ‘High-resolution fault image from accurate
1096 locations and focal mechanisms of the 2008 swarm earthquakes in West Bohemia, Czech
1097 Republic’, *Tectonophysics*, 590, pp. 189–195. Available at:
1098 <https://doi.org/10.1016/j.tecto.2013.01.025>.

1099 Wang, K. *et al.* (2020) ‘Rupture Process of the 2019 Ridgecrest, California Mw 6.4 Foreshock and
1100 Mw 7.1 Earthquake Constrained by Seismic and Geodetic Data’, *Bulletin of the*
1101 *Seismological Society of America*, 110(4), pp. 1603–1626. Available at:
1102 <https://doi.org/10.1785/0120200108>.

1103 Wang, X. and Zhan, Z. (2020) ‘Seismotectonics and Fault Geometries of the 2019 Ridgecrest
1104 Sequence: Insight From Aftershock Moment Tensor Catalog Using 3-D Green’s Functions’,
1105 *Journal of Geophysical Research: Solid Earth*, 125(5), p. e2020JB019577. Available at:
1106 <https://doi.org/10.1029/2020JB019577>.

1107 Wesnousky, S.G. (2005) ‘The San Andreas and Walker Lane fault systems, western North
1108 America: transpression, transtension, cumulative slip and the structural evolution of a major
1109 transform plate boundary’, *Journal of Structural Geology*, 27(8), pp. 1505–1512. Available
1110 at: <https://doi.org/10.1016/j.jsg.2005.01.015>.

1111 Wollherr, S., Gabriel, A.-A. and Mai, P.M. (2019) ‘Landers 1992 “Reloaded”’: Integrative
1112 Dynamic Earthquake Rupture Modeling’, *Journal of Geophysical Research: Solid Earth*,
1113 124(7), pp. 6666–6702. Available at: <https://doi.org/10.1029/2018JB016355>.

1114 Xu, X. *et al.* (2016) ‘Refining the shallow slip deficit’, *Geophysical Journal International*, 204(3),
1115 pp. 1867–1886. Available at: <https://doi.org/10.1093/gji/ggv563>.

1116 Yang, W., Hauksson, E. and Shearer, P.M. (2012) ‘Computing a Large Refined Catalog of Focal
1117 Mechanisms for Southern California (1981–2010): Temporal Stability of the Style of
1118 Faulting’, *Bulletin of the Seismological Society of America*, 102(3), pp. 1179–1194.
1119 Available at: <https://doi.org/10.1785/0120110311>.

1120 Zhang, Z. *et al.* (2020) ‘A Dynamic-Rupture Model of the 2019 Mw 7.1 Ridgecrest Earthquake
1121 Being Compatible with the Observations’, *Seismological Research Letters*, 92(2A), pp.
1122 870–876. Available at: <https://doi.org/10.1785/0220200258>.

1123 Zoback, M.D. *et al.* (1987) ‘New Evidence on the State of Stress of the San Andreas Fault System’,
1124 *Science*, 238(4830), pp. 1105–1111. Available at:
1125 <https://doi.org/10.1126/science.238.4830.1105>.

1126